

# Weighing the Giants I. Weak-lensing masses for 51 massive galaxy clusters: project overview, data analysis methods and cluster images

Anja von der Linden<sup>1,2,3</sup>  $\star$ , Mark T. Allen<sup>1,2</sup>, Douglas E. Applegate<sup>1,2,4,5</sup>, Patrick L. Kelly<sup>1,2,4,6</sup>, Steven W. Allen<sup>1,2,4</sup>, Harald Ebeling<sup>7</sup>, Patricia R. Burchat<sup>1,2</sup>, David L. Burke<sup>1,4</sup>, David Donovan<sup>7</sup>, R. Glenn Morris<sup>1,4</sup>, Roger Blandford<sup>1,2,4</sup>, Thomas Erben<sup>5</sup>, Adam Mantz<sup>8,9</sup>

<sup>1</sup>Kavli Institute for Particle Astrophysics and Cosmology, Stanford University, 452 Lomita Mall, Stanford, CA 94305-4085, USA

<sup>2</sup>Department of Physics, Stanford University, 382 Via Pueblo Mall, Stanford, CA 94305-4060, USA

<sup>3</sup>Dark Cosmology Centre, Niels Bohr Institute, University of Copenhagen, Juliane Maries Vej 30, 2100 Copenhagen Ø, Denmark

<sup>4</sup>SLAC National Accelerator Laboratory, 2575 Sand Hill Road, Menlo Park, CA 94025, USA

<sup>5</sup>Argelander-Institut für Astronomie, Universität Bonn, Auf dem Hügel 71, 53121 Bonn, Germany

<sup>6</sup>Department of Astronomy, University of California, B-20 Hearst Field Annex # 3411 Berkeley, CA 94720-3411, USA

<sup>7</sup>Institute for Astronomy, 2680 Woodlawn Drive, Honolulu, HI 96822, USA

<sup>8</sup>Kavli Institute for Cosmological Physics, University of Chicago, 5640 South Ellis Avenue, Chicago, IL 60637-1433, USA

<sup>9</sup>Department of Astronomy and Astrophysics, University of Chicago, 5640 South Ellis Avenue, Chicago, IL 60637-1433, USA

Accepted 2013 October 9. Received 2013 October 2; in original form 2012 August 1

## ABSTRACT

This is the first in a series of papers in which we measure accurate weak-lensing masses for 51 of the most X-ray luminous galaxy clusters known at redshifts  $0.15 \lesssim z_{\text{Cl}} \lesssim 0.7$ , in order to calibrate X-ray and other mass proxies for cosmological cluster experiments. The primary aim is to improve the absolute mass calibration of cluster observables, currently the dominant systematic uncertainty for cluster count experiments. Key elements of this work are the rigorous quantification of systematic uncertainties, high quality data reduction and photometric calibration, and the “blind” nature of the analysis to avoid confirmation bias. Our target clusters are drawn from X-ray catalogs based on the ROSAT All-Sky Survey, and provide a versatile calibration sample for many aspects of cluster cosmology. We have acquired wide-field, high-quality imaging using the Subaru and CFHT telescopes for all 51 clusters, in at least three bands per cluster. For a subset of 27 clusters, we have data in at least five bands, allowing accurate photometric redshift estimates of lensed galaxies. In this paper, we describe the cluster sample and observations, and detail the processing of the SuprimeCam data to yield high-quality images suitable for robust weak-lensing shape measurements and precision photometry. For each cluster, we present wide-field three-color optical images and maps of the weak-lensing mass distribution, the optical light distribution, and the X-ray emission. These provide insights into the large-scale structure in which the clusters are embedded. We measure the offsets between X-ray flux centroids and the Brightest Cluster Galaxies in the clusters, finding these to be small in general, with a median of 20 kpc. For offsets  $\lesssim 100$  kpc, weak-lensing mass measurements centered on the Brightest Cluster Galaxies agree well with values determined relative to the X-ray centroids; miscentering is therefore not a significant source of systematic uncertainty for our weak-lensing mass measurements. In accompanying papers we discuss the key aspects of our photometric calibration and photometric redshift measurements (Kelly et al.), and measure cluster masses using two methods, including a novel Bayesian weak-lensing approach that makes full use of the photometric redshift probability distributions for individual background galaxies (Applegate et al.). In subsequent papers, we will incorporate these weak-lensing mass measurements into a self-consistent framework to simultaneously determine cluster scaling relations and cosmological parameters.

**Key words:** galaxies: clusters: general; gravitational lensing: weak; methods: data analysis; cosmology: observations; galaxies: elliptical and lenticular, cD

## 1 INTRODUCTION

The formation of cosmic structure depends sensitively on the mass and energy content of the Universe, and the physical nature of dark matter and dark energy. Galaxy clusters are the most massive gravitationally bound structures, sitting at the largest nodes of the cosmic web. As such, their number density, baryon content, and evolution are sensitive probes of cosmological parameters, in particular the amplitude of matter fluctuations ( $\sigma_8$ ), the mean matter and dark energy densities ( $\Omega_m$  and  $\Omega_{DE}$ ), and the dark energy equation of state parameter ( $w$ ) (for a recent review, see Allen et al. 2011).

The idea of “counting clusters” as a way to test cosmology has existed for decades (e.g., Kaiser 1984; Henry & Arnaud 1991). The discovery of massive clusters at high redshifts (Donahue et al. 1998; Bahcall & Fan 1998) provided supporting evidence for a low matter density Universe, and presaged the discovery of dark energy from Type Ia supernovae studies (Riess et al. 1998; Perlmutter et al. 1999). Cluster counts paved the way in determining the now accepted value of  $\sigma_8 \sim 0.8$  (e.g. Borgani et al. 2001; Schuecker et al. 2003). Recently, measurements of the evolution of the cluster number density have provided some of the most precise and robust constraints on dark energy (Vikhlinin et al. 2009b; Mantz et al. 2010a), as well as departures from General Relativity on cosmological scales (Rapetti et al. 2010, 2013; Schmidt et al. 2009), and the species-summed neutrino mass (Mantz et al. 2010c; Reid et al. 2010).

A fundamental challenge for cluster count experiments is that the survey observations do not measure cluster masses directly, but rather a property that correlates with cluster mass, typically with significant associated scatter. For X-ray surveys, the standard survey observable is the X-ray flux, which with the cluster redshift gives the X-ray luminosity; for optical red-sequence finders, survey measures are typically based on optical richness; and for millimeter surveys the typical observable is the Sunyaev-Zel’dovich (SZ) flux. In order to reconstruct the underlying mass function, the scaling relation between the survey observable and cluster mass, as well as the scatter in this relation as a function of mass and redshift, must be measured. This process can be improved if, for a representative subsample of the survey clusters, one can also obtain deeper follow-up measurements of precise mass proxies with lower systematic scatter (Mantz et al. 2010a,b; Vikhlinin et al. 2009a,b). The subsample re-observed need not be large in order to bring a substantial boost in constraining power (Mantz et al. 2010a; Wu et al. 2010).

### 1.1 The role of mass proxies

X-ray observations provide a critical element of this work, offering several observables that are straightforward to measure and which correlate tightly with true cluster mass. For example, the temperature of the intracluster medium,  $T_X$ , traces cluster mass with a scatter of 10–15%, far better than the total X-ray luminosity (scatter  $\sim 40\%$ ). Other X-ray proxies such as gas mass,  $M_{\text{gas}}$ , thermal energy,  $Y_X (= M_{\text{gas}} T_X)$ , and center-excised X-ray luminosity provide comparable or possibly even lower scatter (Allen et al. 2008; Kravtsov et al. 2006; Maughan 2007; Mantz et al. 2010b).

However, even for these low-scatter mass proxies, the absolute scaling with true cluster mass must also be determined, accurately and robustly. For X-ray data, under the assumptions of hydrostatic equilibrium and spherical symmetry, one can relate the observed gas density and temperature profiles to the underlying mass profile. Yet even for the most dynamically relaxed clusters, and at optimal

measurement radii ( $r \sim r_{2500}$ ), hydrostatic X-ray mass estimates are expected to be biased at the 5–10% level due to non-thermal pressure support from residual gas bulk motion and other processes (Nagai et al. 2007; Rasia et al. 2012). For less relaxed systems, and for measurements at larger radii ( $r \gtrsim r_{500}$ ), the biases in hydrostatic measurements can be significantly worse (20–30%, Nagai et al. 2007). This uncertainty in the absolute mass scaling is currently the dominant systematic uncertainty in the constraints on  $\sigma_8$  from cluster counts (Mantz et al. 2010a; Vikhlinin et al. 2009b; Rozo et al. 2010; Sehgal et al. 2011; Benson et al. 2013). In order for future surveys to access their full constraining power, it is imperative to calibrate these mass proxies to within 5% and over the entire mass and redshift range of interest (Wu et al. 2010).

### 1.2 Weak-lensing mass measurements as calibrators for cluster masses

The most promising method currently capable of absolutely calibrating mass measurements for statistical cluster samples is cluster weak gravitational lensing. Weak-lensing mass measurements do not require a baryonic tracer, but directly measure the total gravitating matter. For individual clusters, weak lensing is inherently noisy since the intrinsic ellipticity distribution of galaxies is broad and lensing measurements are sensitive to all structure along the line of sight. Utilizing cluster weak-lensing mass measurements for precision cosmology requires a thorough understanding of the systematic biases involved. Since the shear induced on a background galaxy depends on the cluster mass, the ratios of angular diameter distances between the observer, cluster and source, and cosmology, there are three possible sources of systematic uncertainties. Observationally, biases in the shear measurements and in the redshifts of background galaxies translate to biased mass measurements. Even in the absence of observational biases, systematic uncertainties may arise from the assumptions made to relate the measured lensing signal to an intrinsic cluster mass.

Lensing inherently measures projected, 2D masses; however, to compare these to the halo mass function, they need to be related to 3D masses. The most common method to do so is to fit spherically symmetric density models (such as the NFW profile, Navarro et al. 1997) to the measured shear profiles. Adopting a profile shape has the added advantages that it breaks the mass-sheet degeneracy, and that significantly fewer galaxies are required compared to non-parametric mass reconstruction. (Note that the aperture mass method, which also assumes spherical symmetry but does not directly fit a specific profile, still requires a profile assumption at large radii to break the mass-sheet degeneracy.) However, because clusters are generally triaxial, the assumption of spherical symmetry leads to over-/underestimates of the mass if the cluster major axis is aligned along/perpendicular to the line of sight (Corless & King 2007; Meneghetti et al. 2010). Mass in the infall region of clusters (e.g., filaments and infalling groups) and/or unassociated structures along the line of sight can similarly bias individual mass measurements (Hoekstra 2001, 2003). Quantifying the expected scatter due to these sources, as well as any expected bias due to the profile assumption, can be achieved straightforwardly from cosmological N-body simulations, by applying the same mass measurement methods to the simulations as to the real data. For the NFW profile (or closely related profiles), this has recently been done by a number of groups (Becker & Kravtsov 2011; Oguri & Hamana 2011; Bahé et al. 2012). The intrinsic scatter due to projection effects is found to be  $\sim 25\%$  (Becker & Kravtsov 2011; Bahé et al. 2012), while the expected bias is dependent on the outer fit radius – if this is re-

stricted to be close to the virial radius, the average mass can be recovered with little bias (Becker & Kravtsov 2011; Oguri & Hamana 2011).

The unbiased mean, yet considerable intrinsic scatter, for cluster weak lensing measurements implies that relatively large samples of clusters are necessary to meet the calibration needs of cluster cosmology. For such work, the clusters used should ideally be drawn representatively from the surveys in question, so as to have the same selection function. This is a fundamental reason why, for example, strong-lensing selected clusters should not be used for this purpose – the incidence of strong lensing is highly biased towards clusters that are elongated and/or have additional structures along the line of sight.

To date, only a handful of studies have measured individual weak-lensing masses for more than a few clusters, and none have fully incorporated the results into a robust cosmological work, which would require solving simultaneously for the scaling relations and cosmological parameters (Mantz et al. 2010a; Allen et al. 2011). A number of early works (Allen 1998; Hjorth et al. 1998; Cypriano et al. 2004; Smith et al. 2005) compared lensing mass estimates of massive clusters to X-ray mass proxies, but the weak-lensing mass measurements were generally limited by the small fields of view of existing cameras. The work of Dahle et al. (2002, see also Dahle 2006; Pedersen & Dahle 2007) provides the so-far largest compilation of weak-lensing mass measurements of individual clusters (38 clusters). With the increasing availability of high-quality, wide-field mosaic cameras, the precision of weak-lensing mass measurements at sufficiently large cluster radii has significantly increased, providing the means to study cluster scaling relations with total mass measurements. Hoekstra (2007) compared weak-lensing masses of 20 clusters, derived from two-filter optical imaging, to independently measured X-ray luminosities and temperatures, as well as galaxy velocity dispersions. For 18 of these clusters, Mahdavi et al. (2008) computed X-ray hydrostatic masses and compared these to the weak-lensing mass estimates. Bardeau et al. (2007) compared weak-lensing masses for 11 clusters measured from three-filter imaging to X-ray luminosities and temperatures. The LoCuSS project measured weak-lensing masses with two-filter imaging for 30 clusters (Okabe et al. 2010a). For 12 of them, the lensing masses were compared to  $T_X$ ,  $M_{\text{gas}}$ , and  $Y_X$  (Okabe et al. 2010b) as well as hydrostatic mass estimates (Zhang et al. 2010). Using 18 of these clusters, Marrone et al. (2012) present a first comparison of integrated Compton parameters from SZ observations to weak-lensing mass determinations. High et al. (2012) present a second SZ–weak lensing comparison for 5 clusters. Hoekstra et al. (2011) used single-filter Hubble Space Telescope observations to measure weak-lensing masses for 25 clusters of moderate X-ray luminosity, and compared these to the cluster X-ray luminosities and temperatures. For larger samples of less massive systems, stacking analyses enable the determination of the mean cluster mass in bins of survey observable (Johnston et al. 2007; Leauthaud et al. 2010). For most studies listed here, the bulk of the cluster samples studied is at  $z_{\text{Cl}} \sim 0.2 - 0.3$ . A few studies have specifically targeted higher-redshift clusters, both using space-based (Jee et al. 2011, 22 clusters at  $z \gtrsim 1$ ) and ground-based imaging (Israel et al. 2012, 7 clusters at  $z \sim 0.4 - 0.8$ ).

A key assumption of these pathfinding lensing studies is to implicitly place all background galaxies at the same effective redshift. For low-redshift clusters ( $z_{\text{Cl}} \sim 0.2$ , representing the bulk of the clusters studied to date), this approximation should not severely bias the mass measurements; the peak of the galaxy distribution is at  $z \sim 0.8 - 1.0$  and, for clusters at low redshifts, the shear signal

varies only slowly over this range, causing errors in the effective redshift to bias the mass only slightly. For clusters at higher redshifts ( $z_{\text{Cl}} \gtrsim 0.4$ ), however, this is no longer the case and one can significantly reduce systematic scatter and potential bias (in case the assumed redshift distribution is not representative of the redshift distribution in cluster fields) by incorporating appropriate redshift information for individual galaxies. Since weak lensing is based on shape measurements of many faint galaxies, this is feasible only with photometric redshifts. Current and up-coming cluster surveys, such as the South Pole Telescope survey (SPT, Vanderlinde et al. 2010), the Atacama Cosmology Telescope (ACT, Sehgal et al. 2011), Planck (Planck Collaboration et al. 2011), the Dark Energy Survey (The Dark Energy Survey Collaboration 2005, DES), and eROSITA (Predehl et al. 2010) will find hundreds to many thousands of massive clusters in the redshift range  $0.5 \lesssim z \lesssim 1.5$ . Lensing mass calibrations for these surveys will be vital to maximizing their potential to constrain cosmology. It is therefore essential to develop the strategies and tools to measure unbiased cluster masses using photometric redshifts in an optimal way.

### 1.3 This study

In this series of papers, we develop and apply techniques to enable the determination of accurate weak-lensing masses for a total of 51 clusters from deep, high-quality multi-color Subaru SuprimeCam and CFHT MegaPrime optical imaging.

In this first paper, we describe the cluster sample and the data reduction methods: a careful data treatment is key to robust shear and photometry measurements, and unbiased cluster mass determination. We discuss the correspondence between the dark matter, gas, and optical light distributions, and the relation of the positions of the Brightest Cluster Galaxies (BCGs) and X-ray centroids. In Paper II (Kelly et al. 2014), we describe the details of our photometric calibration, including a prescription to construct the “star flat”, which corrects flat-field errors due to varying pixel scale and scattered light in wide-field cameras. In Paper II we also describe an improved and versatile technique to calibrate photometric zero-points from stellar colors, whose implementation we have made publicly available. Using these methods, we show that we can estimate robust photometric redshifts even when calibration data are lacking, and present an initial analysis of the source-redshift dependent shear signal of the clusters. In Paper III (Applegate et al. 2014) we introduce a novel Bayesian approach to weak-lensing mass estimation that makes full use of photometric redshift probability distributions of lensed galaxies. We compare the obtained masses to those derived from the more common method of adopting a single effective redshift for the background galaxies. Critically, we also include a detailed discussion and quantification of the systematic uncertainties involved. Additional papers will focus on the scaling relations between weak-lensing masses and other observables, and present updated cosmological constraints.

For a project such as this, where a central goal is the comparison of measurements determined by independent techniques, and where the measurements to be calibrated have already been used in cosmological studies, there is a clear danger of “observer bias” or “confirmation bias”. These biases are well-known in the wider physics community, and can be avoided by implementing “blind analyses” (Klein & Roodman 2005). While blind analyses have not yet been used widely in astronomy to date, they will be essential for upcoming precision cosmology measurements (see also Allen et al. 2011; Croft & Dailey 2011). To combat confirmation bias, we have chosen to explicitly avoid direct comparison with X-ray mass

proxies, or indeed any other mass estimates, during the course of this study, revealing all comparisons only at the end of a given part of the study. To enforce this restriction, in the few cases where intermediate results were presented, all non-lensing mass estimates were multiplied by a random, unrevealed number (all masses were multiplied by the same number), thus removing the absolute scalings of the lensing vs. other mass relations, the primary quantities of interest. Since the lensing data are not altered, this procedure allows complete and accurate analyses of statistical and systematic errors, while eliminating unintentional bias towards the expected correlation with other mass proxies.

In the very early stages of this work blinding was not implemented and preliminary comparisons of crude mass estimates for a small fraction ( $\lesssim 20$  per cent) of the clusters were examined. We emphasize, however, that the final, more sophisticated mass measurement methods described in Paper III were developed independently of these early analyses and that all lensing mass measurements presented in these papers were determined blindly with respect to other mass proxies and all results in the literature. "Unblinding" with respect to lensing mass estimates in the literature took place only after the lensing analysis was completed, including internal review of Papers I-III. "Unblinding" with respect to X-ray and other independent mass proxies has not occurred at the time of completing papers I-III. Any subsequent changes to the lensing analysis will be reported in Paper III, or later work, if necessary.

This paper is structured as follows: In Sect. 2 we describe the cluster sample and the optical imaging observations. Since the lensing analysis is performed mostly on SuprimeCam data, we give a detailed description of the SuprimeCam data reduction in Sect. 3 (with additional details in App. A). Sect. 4 describes the object detection and initial photometry measurements. In Sect. 5 we briefly summarize the shear measurement method based on Kaiser et al. (1995), discuss our strategies to correct for the anisotropy (also App. B) and isotropic smearing of the point spread function, and discuss the calibration using STEP2 simulations (Massey et al. 2007), including accounting for correlated noise. In Sect. 6 and App. C we present a gallery of cluster images and maps of the total mass distribution as recovered from the weak-lensing data, the large-scale structure around each cluster as traced by galaxies on the red sequence, and the X-ray emission associated with the cluster. In Sect. 7, we investigate the impact of different choices for the cluster centers on the lensing results. We summarize and provide an outlook on future work in Sect. 8.

The fiducial cosmology adopted in this paper is a flat  $\Lambda$ CDM model with  $\Omega_m = 0.3$  and  $H_0 = 100 h$  km/s/Mpc, where  $h = 0.7$ .

## 2 CLUSTER SAMPLE

We have acquired deep wide-field observations in at least three filters for a total of 51 clusters. Predominantly, these images were taken as part of a dedicated program (Donovan 2007) to image clusters selected from two cluster samples constructed from the Rosat All Sky Survey (RASS, Truemper 1993), namely the Massive Cluster Survey (MACS; Ebeling et al. 2001, 2007, 2010) and the Brightest Cluster Survey (BCS; Ebeling et al. 1998, 2000). The clusters were observed with SuprimeCam on the Subaru telescope, and with MegaPrime on the Canada-France-Hawaii Telescope (CFHT) for  $u$ -band imaging. We supplemented these data with further imaging from the SuprimeCam and CFHT data archives, where available. In addition, we searched the archives for multi-color imaging of the sample of relaxed clusters defined by Allen et al.

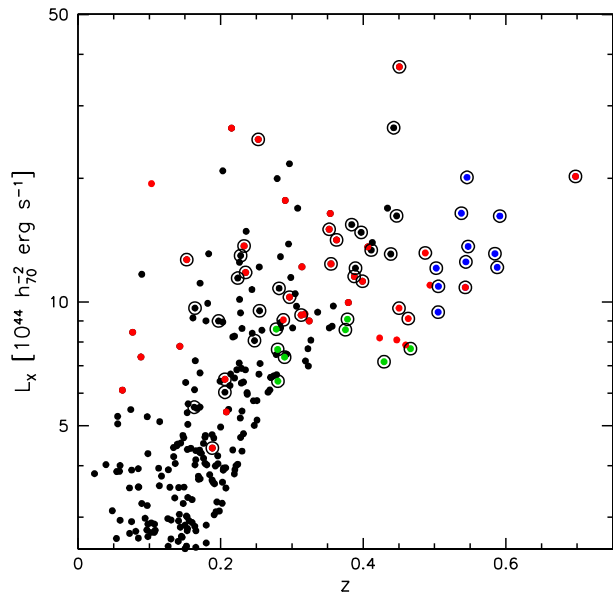


**Figure 1.** X-ray luminosities (in the fiducial cosmology) vs. redshifts of clusters in the M10 cosmology sample (black), the high- $z$  MACS sample (blue), and the A08 sample of relaxed clusters (red). Clusters for which we derive weak-lensing mass measurements are marked with large open circles. Clusters that are in the weak lensing sample, but not in one of the three main sample are shown in green (see text for details). Clusters that belong to both the relaxed sample and the cosmology sample or the high- $z$  sample are marked as relaxed clusters. (Note that the cosmology sample and high- $z$  sample are disjoint.)

(2008, hereafter A08). For the SuprimeCam data reduction, we made use of additional "empty fields" (extragalactic fields without bright stars or large foreground galaxies) taken at approximately the same epoch as our observations (Sect. 3.1.2); these data include an additional three clusters (A1758, A370, and RXJ0142.0+2131).

The clusters included in this sample span a wide range in redshift ( $0.15 < z_{cl} < 0.7$ ), as well as dynamical state. As such, several (overlapping) subsamples can be identified which are of particular interest to various aspects of cluster cosmology. For instance, 28 of the clusters are included in the cosmological analysis of Mantz et al. (2010a,b, hereafter jointly referred to as M10), which used clusters selected from the BCS, the ROSAT-ESO Flux Limited X-ray (REFLEX, Böhringer et al. 2004), and MACS. In future work, we will incorporate our lensing mass measurements for these clusters into our framework to simultaneously determine cosmological parameters and scaling relations between mass proxies and true mass, as measured on average by the weak-lensing masses. Relaxed clusters are of special interest for investigating the bias in X-ray hydrostatic mass estimates. For this reason our sample includes 18 dynamically relaxed clusters from the A08 sample, 13 of which are in common with the M10 sample. The sample also contains all 12 clusters above  $z > 0.5$  in the Faint MACS sample (Ebeling et al. 2007). Although these are not actually part of the M10 sample, their calibration is particularly interesting for future work with newer, larger cluster surveys. Our study is the first effort to calibrate mass measurements with ground-based weak lensing at these redshifts. An additional seven clusters in the sample do not belong to any of these three categories. Note that a significant fraction of the data taken for the *Weighing the Giants* project is cur-

**Table 1.** Overview of the cluster sample. The columns are (1) cluster name; (2) redshift; (3) right ascension and (4) declination (both in J2000) of the X-ray centroid; (5) the filters in which the cluster was observed (see Table 2 for filter and instrument details); (6) the image(s) used as lensing band, with effective exposure time in seconds and seeing in arcsec. Column (7) indicates whether the cluster is part of the sample of Mantz et al. (2010a,b, ; M10); if so, the parent survey is also listed. Column (8) indicates whether the cluster is relaxed and in the Allen et al. (2008, ; A08) sample. The table is sorted by increasing cluster redshifts, which are compiled from the MACS (Ebeling et al. 2007, 2010; Mann & Ebeling 2012), BCS (Ebeling et al. 1998), and REFLEX (Böhringer et al. 2004) catalogs.

Cluster	$z_{Cl}$	R.A. (J2000)	Dec. (J2000)	Filter Bands	Lensing Band (exp. time [s], seeing ["])	M10 Sample	A08 Sample
(1)	(2)	(3)	(4)	(5)	(6)	(7)	(8)
A2204	0.152	16:32:47.158	05:34:33.00	$B_J V_J R_C g^* r^*$	$V_J$ (1038, 0.58)	BCS	√
A750	0.163	09:09:12.653	10:58:34.74	$V_J R_C i^+$	$V_J$ (1728, 0.72)	BCS	-
RXJ1720.1+2638	0.164	17:20:09.996	26:37:28.70	$B_J V_J R_C i^+$	$V_J$ (972, 0.51)	BCS	-
A383	0.188	02:48:03.268	-03:31:46.43	$B_J V_J R_C i^+ z^+ u^*$	$i^+$ (2160, 0.58)	REFLEX	√
A209	0.206	01:31:53.139	-13:36:48.35	$V_J R_C i^+$	$i^+$ (1188, 0.55)	REFLEX	-
A963	0.206	10:17:03.562	39:02:51.51	$V_J R_C I_C$	$I_C$ (2700, 0.61)	BCS	√
A2261	0.224	17:22:26.986	32:07:57.89	$B_J V_J R_C u^* g^* r^*$	$R_C$ (1440, 0.55)	BCS	-
A2219	0.228	16:40:20.340	46:42:30.00	$B_J V_J R_C I_{12}$	$V_J$ (924, 0.49)	BCS	-
A2390	0.233	21:53:37.070	17:41:45.39	$B_J V_J R_C I_C i^+ z^+ u^*$	$R_C$ (3420, 0.56)	BCS	√
RXJ2129.6+0005	0.235	21:29:39.727	00:05:18.15	$B_J V_J R_C i^+$	$V_J$ (1863, 0.58)	BCS	√
A521	0.247	04:54:07.408	-10:13:24.29	$B_J V_J R_C i^+ z^+ g^* r^*$	$R_C$ (1428, 0.61)	REFLEX	-
A1835	0.253	14:01:01.927	02:52:39.89	$V_J I_C i^+ g^* r^*$	$i^+$ (1944, 0.91)	BCS	√
A68	0.255	00:37:05.947	09:09:36.02	$B_J R_C I_C i^+$	$R_C$ (2160, 0.55)	BCS	-
A2631	0.278	23:37:38.330	00:16:14.48	$B_J V_J R_C$	$R_C$ (1296, 0.60)	REFLEX	-
A1758N	0.279	13:32:43.466	50:32:38.33	$B_J R_C z^+ g^* r^*$	$R_C$ (2880, 0.59)	-	-
RXJ0142.0+2131	0.280	01:42:03.311	21:31:22.64	$B_J V_J i^+$	$i^+$ (2136, 0.58)	-	-
A611	0.288	08:00:56.818	36:03:25.52	$B_J V_J R_C I_C g^* r^*$	$I_C$ (1896, 0.62)	-	√
Zw7215	0.290	15:01:22.757	42:20:51.05	$B_J V_J R_C$	$R_C$ (1458, 0.50)	-	-
A2552	0.302	23:11:33.163	03:38:06.50	$B_J V_J R_C$	$R_C$ (1224, 0.59)	MACS	-
MS2137.3-2353	0.313	21:40:15.173	-23:39:39.77	$B_J V_J R_C I_C z^+$	$R_C$ (5562, 0.57)	MACS	√
MACSJ1115.8+0129	0.355	11:15:51.881	01:29:54.98	$V_J R_C I_C$	$R_C$ (1944, 0.65)	MACS	√
RXJ1532.8+3021	0.363	15:32:53.830	30:20:59.38	$B_J V_J R_C I_C z^+ u^*$	$R_C$ (2106, 0.55)	MACS	√
A370	0.375 <sup>b</sup>	02:39:53.246	-01:34:37.84	$B_J R_C I_C i^+ z^+ u^* g^* r^* i^*$	$R_C$ (3240, 0.52)	-	-
MACSJ0850.1+3604	0.378	08:50:06.986	36:04:20.45	$B_J V_J R_C I_C i^+ z^+$	$V_J$ (1944, 0.81)	-	-
MACSJ0949.8+1708	0.384	09:49:51.785	17:07:08.31	$B_J V_J R_C I_C i^+ z^+ u^*$	$V_J$ (1692, 1.02)	MACS	-
MACSJ1720.2+3536	0.387	17:20:16.666	35:36:23.35	$B_J V_J R_C I_C z^+$	$V_J$ (1944, 0.69)	MACS	√
MACSJ1731.6+2252	0.389	17:31:39.192	22:51:49.96	$B_J V_J R_C I_C z^+$	$R_C$ (864, 0.50)	MACS	-
MACSJ2211.7-0349	0.397	22:11:45.907	-03:49:41.94	$B_J V_J R_C I_C z^+ u^*$	$V_J$ (1944, 0.63)	MACS	-
MACSJ0429.6-0253	0.399	04:29:36.001	-02:53:05.63	$V_J R_C I_C$	$R_C$ (2592, 0.73)	MACS	√
RXJ2228.6+2037	0.411	22:28:32.777	20:37:14.58	$B_J V_J R_C I_C z^+$	$R_C$ (864, 0.47)	MACS	-
MACSJ0451.9+0006	0.429	04:51:54.684	00:06:18.52	$B_J V_J R_C I_C$	$R_C$ (2160, 0.62)	-	-
MACSJ1206.2-0847	0.439	12:06:12.293	-08:48:06.22	$V_J R_C I_C z^+ g^* r^* i^* z^*$	$R_C$ (2520, 0.79)	MACS	-
MACSJ0417.5-1154	0.443	04:17:34.320	-11:54:26.65	$V_J R_C I_C$	$R_C$ (2592, 0.74)	MACS	-
MACSJ2243.3-0935	0.447	22:43:21.437	-09:35:42.76	$V_J R_C I_C z^+ u^* g^* r^* i^* z^* B_{12}$	$V_J$ (972, 0.50)	MACS	-
MACSJ0329.6-0211	0.450	03:29:41.459	-02:11:45.52	$B_J V_J R_C I_C z^+ u^*$	$V_J$ (1944, 0.55)	-	√
RXJ1347.5-1144	0.451	13:47:30.778	-11:45:09.43	$B_J V_J R_C I_C z^+ u^* g^* r^* i^* z^*$	$R_C$ (2592, 0.69)	MACS	√
MACSJ1621.3+3810	0.463	16:21:24.749	38:10:09.31	$B_J V_J R_C I_C z^+ u^*$	$I_C$ (1568, 0.52)	-	√
MACSJ1108.8+0906	0.466	11:08:55.154	09:06:02.79	$B_J V_J R_C I_C$	$V_J$ (1944, 0.86)	-	-
MACSJ1427.2+4407	0.487	14:27:16.025	44:07:30.51	$V_J R_C z^+$	$R_C$ (2544, 0.59)	-	√
MACSJ2214.9-1359	0.502	22:14:57.310	-14:00:11.39	$B_J V_J R_C I_C z^+ u^*$	$R_C$ (2592, 0.52)	-	-
MACSJ0257.1-2325	0.505	02:57:09.089	-23:26:03.90	$B_J V_J R_C I_C z^+ u^*$	$V_J$ (1080, 0.59)	-	-
MACSJ0911.2+1746	0.505	09:11:10.870	17:46:31.38	$B_J V_J R_C I_C i^+ z^+$	$V_J$ (1908, 0.50)	-	-
MS0451.6-0305	0.538	04:54:11.444	-03:00:50.76	$B_J V_J R_C I_C i^+ z^+ u^* g^* r^* i^* z^*$	$R_C$ (1944, 0.74)	-	-
MACSJ1423.8+2404	0.543	14:23:47.923	24:04:42.77	$B_J V_J R_C I_C z^+ u^*$	$I_C$ (1944, 0.73)	-	√
MACSJ1149.5+2223	0.544	11:49:35.426	22:24:03.62	$B_J V_J R_C I_C i^+ z^+ u^*$	$V_J$ (1620, 0.54)	-	-
MACSJ0717.5+3745	0.546	07:17:32.088	37:45:20.94	$B_J V_J R_C I_C i^+ z^+ u^* g^* r^*$	$V_J$ (1728, 0.55)	-	-
CL0016+16	0.547	00:18:33.445	16:26:13.00	$B_J V_J R_C I_C z^+ u^* g^* r^* i^* z^*$	$V_J$ (5184, 0.62)	-	-
MACSJ0025.4-1222	0.585	00:25:29.907	-12:22:44.64	$B_J V_J R_C I_C z^+ u^*$	$V_J$ (1944, 0.54)	-	-
MACSJ2129.4-0741	0.588	21:29:25.723	-07:41:30.84	$B_J V_J R_C z^+$	$R_C$ (3354, 0.59)	-	-
MACSJ0647.7+7015	0.592	06:47:49.682	70:14:56.05	$B_J V_J R_C I_C i^+ z^+$	$R_C$ (2592, 0.62)	-	-
MACSJ0744.8+3927	0.698	07:44:52.310	39:27:26.80	$B_J V_J R_C I_C i^+ z^+ u^*$	$R_C$ (4869, 0.56)	-	√
MACSJ1931.8-2634 <sup>a</sup>	0.352	19:31:49.608	-26:34:33.60	$B_J V_J R_C I_C z^+$	$R_C$ (2592, 0.73)	MACS	√

<sup>a</sup> High stellar density (Galactic bulge); only used for detailed PSF analysis and investigating the position of the BCG relative to the X-ray emission, not in the lensing analysis.

<sup>b</sup> Redshift taken from the NASA/IPAC Extragalactic Database (NED).

**Table 2.** Overview of the filters used in this work. Note that the response functions of the Subaru Johnson/Cousins filters are considerably more top-hat-like than the original Johnson/Cousins filter functions, making them well suited for photometric redshift determination.

Instrument / Telescope	Short Filter Name	Long Filter Name
SuprimeCam @ Subaru	$B_J$	Johnson $B$ -band
	$V_J$	Johnson $V$ -band
	$R_C$	Cousins $R$ -band
	$I_C$	Cousins $I$ -band
	$i^+$	SDSS $i$ -band
	$z^+$	SDSS $z$ -band
MegaPrime @ CFHT	$u^*$	SDSS $u$ -band
	$g^*$	SDSS $g$ -band
	$r^*$	SDSS $r$ -band
	$i^*$	SDSS $i$ -band
	$z^*$	SDSS $z$ -band
CFH12K @ CFHT	$B_{12}$	Johnson $B$ -band
	$I_{12}$	Cousins $I$ -band

rently being analyzed independently by the CLASH collaboration (Postman et al. 2012; Umetsu et al. 2012).

Fig. 1 illustrates these target clusters in a plot of X-ray luminosity vs. redshift for the parent samples, marking those clusters included in this study. Table 1 summarizes the cluster sample and the multi-color data used in this work. The lensing band is chosen as the deepest image (i.e. the image with the highest number density of objects) with the best seeing from the SuprimeCam  $V_J$ ,  $R_C$ ,  $I_C$ ,  $i^+$ , and MegaPrime  $r^*$  images (see Sect. 3.2).

### 3 DATA REDUCTION

The basis for our data reduction is the GABODS/THELI pipeline (Erben et al. 2005, with additional features described in Schirmer 2013), which is optimized for processing multi-chip mosaic-camera data to produce weak-lensing quality final images. The bulk of our data, especially the lensing band exposures, are from SuprimeCam. Below we describe adaptations of the GABODS/THELI pipeline to the SuprimeCam images analysis. We follow the terminology of Erben et al. (2005), and refer the reader to that work for more in-depth discussions of the standard reduction steps.

To pre-process the MegaPrime datasets, we use the highly automated pipeline of Erben et al. (2009). For a few clusters, we also include data gathered with the CFH12K camera at the CFHT, which are processed with the standard version of the GABODS/THELI pipeline.

For the data processing description, it is helpful to distinguish between *run*-specific steps, which refer to data grouped according to when it was observed (e.g. single nights, or in our case, periods of a few months), and *set*-specific processing, which is applied to all observations of a single field. In Sect. 3.1 we describe the main aspects of the run-specific pre-processing; in Sect. 3.2 we describe the subsequent set-specific steps of the data reduction.

#### 3.1 Pre-processing of SuprimeCam data

SuprimeCam (Miyazaki et al. 2002) is one of the best-suited instruments for cluster weak-lensing observations. The large aperture of the Subaru telescope (8.2 m; Iye et al. 2004), along with the

typically good seeing at Mauna Kea (median seeing 0.7–0.8 arcsec Miyazaki et al. 2002), enable robust shape measurements of faint galaxies with modest exposure times. The field of view of  $34' \times 27'$  is well matched for observing massive clusters at  $z \gtrsim 0.2$ .

The SuprimeCam detector is a mosaic of 10 CCDs, with  $2048 \times 4092$  pixels each. The camera underwent numerous upgrades in the time period of our observations (2000–2008). Table 3 gives a brief overview of the different camera configurations for our data. In particular, we distinguish between “early” data taken before March 27, 2001, before the mosaic was fully populated, and standard 10-CCD data taken thereafter.

The early data, corresponding to configurations “8” and “9”, are hampered by several defects. The CCDs have noticeably non-linear response – for photometry measurements we correct for this in the central six CCDs (see App. A). The CCDs have several cosmetic defects, and one CCD has a pixel indexing issue, where the central part of the CCD appears offset by  $\sim 0.5''$  (see App. A). Because of these issues, we do not use data from these early configurations for shape measurements.

In March 2001, the CCDs were replaced with 10 newer MIT/Lincoln Labs (LL) CCDs. These CCDs are well suited for weak-lensing purposes, and were used for the bulk of our observations. The only notable issues are the limited dynamic range (the response becomes saturated at  $\sim 35000$  ADUs above the bias level), and the noticeable charge-transfer inefficiency (CTI) and lower quantum efficiency of the top left chip (“w67c1”); this chip was omitted for lensing purposes. These CCDs remained the heart of SuprimeCam until July 2008. Because of an electronics upgrade in August 2002, this period is split into two configurations “10.1” and “10.2”. In July 2008, the CCDs were replaced with Hamamatsu Photonics chips, as prototypes for HyperSuprimeCam. These have the unusual artefact that the pixels vary in shape and size; the divisions between pixels are not straight lines, but are curved (S. Miyazaki, private communication). These chips do not suffer from the low saturation level of the previous CCD generation, but the non-linearity is about 1% over the full range – this is noticeable if the flat-field does not have similar counts to the science data. Because we have only a single night of data from this “10.3” configuration, we do not use these data for our lensing analysis.

Each change in camera configuration requires independent data reduction set-up. Additionally, we split the data into epochs of a few months, over which the flat-fields are quite stable (see discussion in Sect. 3.1.2). For each epoch, we download additional bias frames, flat-fields, and empty fields to be used for the super-flat (a flat-field derived from “empty field” night-sky observations, Sect. 3.1.2), from the SMOKA archive (Baba et al. 2002). From these we assemble the master calibration frames for each epoch.

##### 3.1.1 Overscan, bias, & dark corrections

The first data reduction step is the subtraction of the *bias*, i.e. the expected counts in an exposure of zero seconds. The bias level is corrected in two steps: first, the count levels in the overscan pixels of each frame are measured and subtracted; second, a master bias frame is created by stacking many zero-length exposures (after first subtracting the overscan). This master bias is then subtracted from all frames.

The bias level of SuprimeCam is fairly high ( $\sim 10000$  ADU), but the overscan regions are relatively small ( $\sim 30$ – $80$  pixels). Subtracting the overscan line by line, as done by the GABODS/THELI pipeline, is thus noisy, leading to striped features in the bias frames. All of our science images are taken with broad-band filters; thus the

**Table 3.** Summary of the SuprimeCam configurations spanned by our data. Column (1) gives the identifier we use to refer to a configuration; columns (2) and (3) specify the range of dates each configuration spans. Column (4) lists the number of chips that are read out. Column (5) lists the manufacturer (along with the number of CCDs, if the array is mixed). Column (6) briefly describes the main characteristics / changes from the previous configuration. In column (7) we indicate whether we use a configuration for the lensing shape measurements. The bulk of our data is from configuration 10.2.

Configuration Name (1)	Start Date (2)	End Date (3)	No. of CCDs (4)	CCD Types (5)	Comments (6)	Used for Lensing (7)
8	2000-07-28	2000-11-21	8	MIT/LL (4), SITe (4)	non-linearity	–
9	2000-11-21	2001-03-17	9	MIT/LL (5), SITe (4)	non-linearity	–
10.1	2001-03-17	2002-08-01	10	MIT/LL	new CCDs	✓
10.2	2002-08-02	2008-07-01	10	MIT/LL	new electronics	✓
10.3	2008-07-21	2011-07-02	10	Hamamatsu Photonics	new CCDs; major upgrade	–

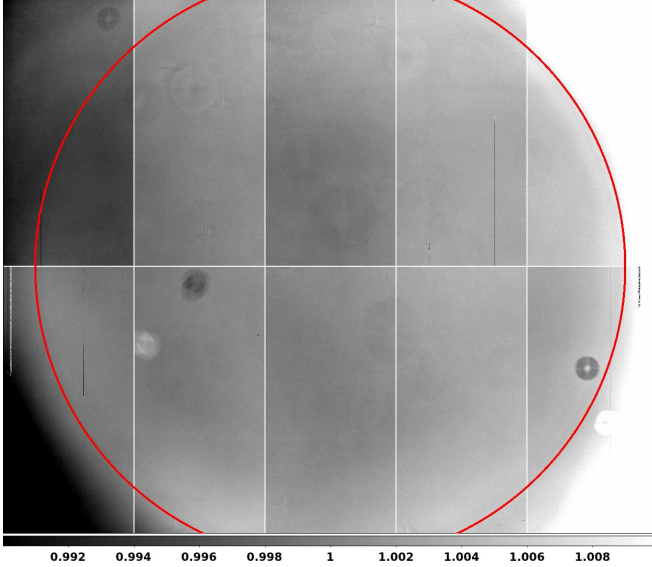


**Figure 2.** Ratio of two flat-fields in the  $R_C$  filter, between two epochs (January - August 2004, and January - April 2005). Within a radius of 15 arcmin (indicated by the red circle), the flat-field pattern is stable to within  $\pm 1\%$ , and differs between epochs only through dust grains on the CCD window or dewar window, visible as ring-shaped features in this flat-field comparison. Beyond the central 15 arcmin, the flat-field is considerably less stable.

absolute sky level (and associated noise) is typically much greater than noise in the bias frames. Hence, noise from the overscan correction is not an issue.

If the image of a bright star happens to fall on the read-out edge of a chip, the overscan is significantly enhanced due to spill-over into the overscan region. When subtracting the overscan for each pixel row, this leads to an oversubtraction. The resulting dark trail of the star is later masked.

To create the master bias, we median-combine the bias frames taken over several months (the same epoch as for the flat-fields; see next section). An exception is configuration 8, where the electronics apparently were adjusted between new moon periods; here each new moon period is treated separately.

For all science and flat-field frames, the appropriate master bias is subtracted. Master dark frames, assembled per camera configuration, are used to identify hot pixels.

### 3.1.2 Flat fields, superflats, fringing

In the second data reduction stage, the counts in science exposures are corrected for varying pixel sensitivity. Each pixel has an intrinsic sensitivity; furthermore, the focal plane of any instrument is inhomogeneously illuminated (areas further from the center receive less light), and the pixel scale varies over the field of view. To correct for different pixel sensitivities, each science frame is divided by a *flat-field*, an image of a uniformly lit source (i.e. no spatial variation over the camera’s field of view).

We follow a two-stage flat-fielding process, as suggested by Erben et al. (2005). In the first step, a master flat-field constructed from median-stacking dedicated domeflat or twilight flat observations is applied. To construct this master flat-field, we downloaded all domeflats and twilight flats available for the timespan of our observations from the SMOKA archive. We investigated the variability of these flat-fields, and even though we find significant variability in the overall illumination pattern between single flats from individual nights, we find that when averaging over several nights, the flat-fields are very stable in time within a radius of  $\sim 15$  arcmin from the center (Fig. 2). Beyond this distance, the field is strongly vignettted – the corners of the field receive only about half as much light as the center. When averaging flat-fields from many months, the corners show variability of the order of 5%. During the analysis of the point spread function (PSF) (Sect. 5.3) we find that the PSF can change rapidly across the vignetting radius. Because of this and the flat-field problems, we mask all pixels beyond a radius of 15 arcmin.

For the master flat-fields, we average the available flat-field exposures to epochs of several months each. For each epoch of science observations, we divide the science images by the appropriate master flat-field. These flat-fields correct the pixel-to-pixel response variation, as well as the large-scale illumination (but see below and Sect. 3.1.4). When both domeflats and twilight flats are available, we use the one that yields flatter corrected science frames.

Flat-fields constructed from domeflats and skyflats correct the pixel-to-pixel response variation, but can leave residual chip-scale response variations of the order of 3% (Erben et al. 2005). In the second flat-fielding step, we correct these with a *superflat*, which is constructed from night-time observations of “empty fields” – fields where the objects are significantly smaller than the chip sizes. Most of our cluster fields are “empty” and can be used in the construction of the superflat; exceptions are fields with very bright foreground stars and their reflections within the optical path. However, multiple exposures of the same field, taken at approximately the same time, are subject to similar gradients in the sky background, reflections within the telescope, etc. To mitigate these effects, we downloaded

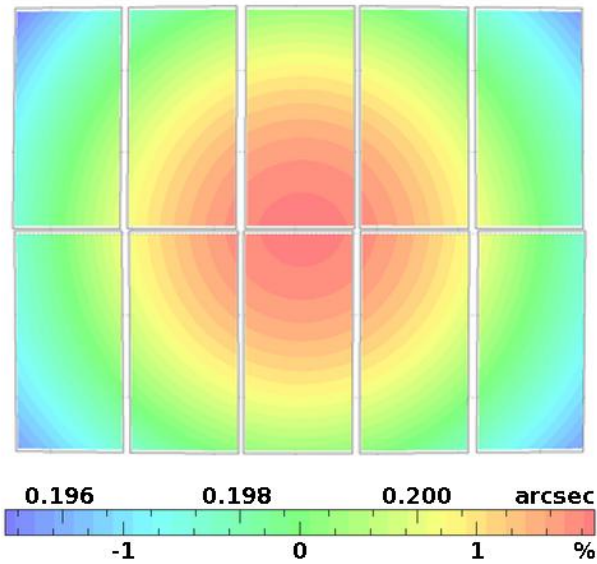


**Figure 3.** A typical distortion pattern of the SuprimeCam focal plane, determined with SCAMP. The figure shows the relative positions of the CCDs on the sky. The local pixel scale has been color-coded in order to illustrate the variation of the mapping between sky coordinates and detector coordinates. The overall variation is within  $\pm 1.5\%$  of the average pixel scale, and its spatial variation can be well described by a third-order polynomial.

additional empty field observations, taken within a few months of our own observations, from the SMOKA archive.

The superflat is constructed by stacking empty field images (each flat-fielded as described above) where detected objects are removed (see Erben et al. 2005, for details). The stacked image is then heavily smoothed and applied as a multiplicative correction to the flat fielded images.

The superflat also provides the basis for correcting fringing (interference patterns in thinned CCDs) in the  $I_C$ ,  $i^+$ , and  $z^+$  exposures. We find that the method of Erben et al. (2005) works well on the SuprimeCam data.

### 3.1.3 Initial astrometric & photometric solution

We determine an initial astrometric solution for the images in order to identify objects across exposures for the star-flat correction (see next section and Paper II). We use SExtractor (Bertin & Arnouts 1996) to extract object catalogs for all observations of the same target field (from all observation nights and filters). For SuprimeCam images, we include saturated objects in these catalogs since, due to the low saturation threshold, there is generally very little overlap in magnitude range between astrometric reference catalogs and the unsaturated objects in our exposures.

We use SCAMP (Bertin 2006) to simultaneously find the astrometric solution for all observations of a given field. Where available, the fields are cross-matched to the Sloan Digital Sky Survey (SDSS DR6; Adelman-McCarthy et al. 2008), and otherwise to the Two Micron All Sky Survey (2MASS; Skrutskie et al. 2006). The robustness of the astrometric solution is judged from the contrast value of the highest peak in the cross-correlation of the catalogs (reported by SCAMP), and the distortion patterns of all input configurations. These should have a regular shape as shown in Fig. 3; false solutions produce patterns that deviate strongly from this. To aid SCAMP in finding the correct astrometric solution, we con-

structed typical linear astrometric headers for each camera configuration and rotation (for many of our exposures, the camera was rotated by  $90^\circ$  between exposures) from fields with robust astrometric solutions derived from matching to SDSS. These are substituted for the original image headers, and greatly expedite the process of finding the best astrometric solution.

### 3.1.4 The star-flat

In the previous steps, we took care to construct a flat-field to accurately calibrate the response of the camera to illumination from a uniformly bright sky. However, for wide-field cameras, this is not a map of the actual sensitivities of all pixels: On the one hand, the pixel scale (and therefore the area each pixel subtends on the sky) can vary by several percent over the field of view (Fig. 3), breaking the underlying assumption of traditional flat-field procedures that each pixel is the same size and therefore should receive the same amount of light. Furthermore, light from a number of sources (the sky itself, the lamps illuminating the dome-flat screen, etc.) is scattered into the camera (Magnier & Cuillandre 2004). The center of the focal plane is more exposed than the edges, and so this additional light contribution affects the center of the image most. The standard flat-field procedure thus overestimates the sensitivity of pixels at field center (as this is where the registered counts are highest). Typical gradients are of the order of 10% for wide-field cameras such as Wide-Field Imager (WFI Koch et al. 2003) at the ESO/MPG 2.2m telescope and MegaPrime (Regnault et al. 2009). This is equivalent to a variation of the zero-point by  $\sim 0.1$  mag across the field, which is an unacceptable systematic error for projects requiring precise photometry, such as ours.

The variation in zero-point across the field can be determined from observations of dense fields of objects with known brightnesses (e.g. from SDSS), or from series of observations with dither patterns that are a significant fraction of the field of view. We use a combination of these two methods to determine the “star-flat”, a correction to the flat-field, for SuprimeCam images, described in detail in Paper II. We find the magnitude of the correction to be similar to other wide-field cameras,  $\sim 10\%$  across the field.

### 3.1.5 Background subtraction

After the star-flat correction, the sky background in the images is no longer uniform. We adapt the procedure of Erben et al. (2005) to handle non-flat backgrounds robustly by extending it to a true “two-pass” method: First, we use the standard SExtractor method to determine the large-scale background, which we then subtract from the image. In the residual image, we identify objects using a very low detection threshold. All pixels belonging to objects are flagged as not-a-number (NaN) in the frame to be corrected, which prevents SExtractor from considering them in the background estimation. We then re-estimate the sky background in these object-blanked frames, and subtract this background frame from the original frame.

### 3.1.6 Stellar halo subtraction

In many of the fields, the brightest stars are surrounded by halos, which stem from reflections from elements along the optical path, such as the dewar window and the filter. The largest such halo has a radius of  $4.7''$ ; i.e. it subtends a noticeable fraction of the SuprimeCam field. Within each annulus of reflected light, the brightness

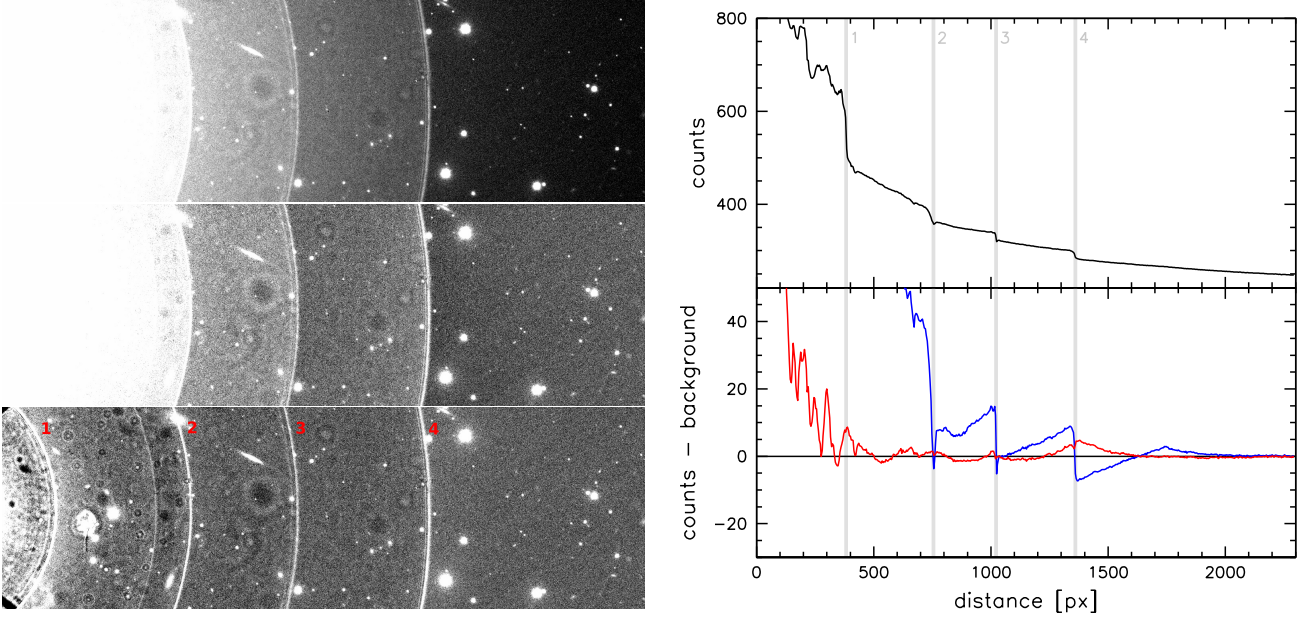


**Figure 4.** Left: Detail of the reflection halos of a bright star. The top panel shows an image cutout before background subtraction, with a bright star to the left. Roughly centered on the star are four reflection halos, whose surface brightness decreases with increasing distance from the star. The transitions between the reflection are marked by bright rings and a sharp drop in surface brightness. The middle panel shows the same image cutout after attempting to subtract the background without removing the stellar halo first. The remaining background is clearly brighter within each halo edge, and darker outside the edges. The bottom panel shows the image after subtracting the stellar halo first, and then proceeding with the general sky subtraction (the color scale is the same for the middle and bottom panels). The sky background is now even across halo boundaries. Right: radial profiles of the background counts, azimuthally averaged around the same bright star as in the images to the left. The top panel shows the background counts before any subtraction: note the distinct steps (marked by the grey vertical lines), and the nearly linear fall-off between the rings. The rings are not precisely concentric; for these profiles, the center of the fourth ring was used. The bottom panel shows the radial profiles after sky subtraction. For the blue profile, the standard sky subtraction was applied without first removing the stellar halo; note the residual saw-tooth pattern extending well beyond the original halo. For the red profile, the stellar halo was subtracted first, and then the background was subtracted. This technique allows us to salvage the area between rings 2 and 4, which would otherwise be lost due to the uneven background. A 100 pixel buffer (indicated by the grey bars in the right panel) around each ring is masked in the lensing image, as well as the area within ring 1. For stars as bright as this one, the area within ring 2 is also masked, as it is considerably noisier, and further artefacts from the reflection halo are visible.

changes only slowly, but the outer edges are marked by brighter rings.

The smoothing length of the background subtraction described above would result in sawtooth residuals across these ring boundaries (Fig. 4), rendering a significant area unusable for reliable object shape measurements (due to non-linear background variations) – we would mask out the entire region within 1500 pixels (5 arcmin) from the star. This would be undesirable and unnecessary, since the areas within the rings have almost uniform backgrounds after flat-fielding. We therefore subtract the reflection halos of the bright stars in the lensing images *before* the background subtraction. This is done with a procedure similar to the one presented in Slater et al. (2009). Preliminary coadded images are examined for stars with visible halos; once these stars are identified, the astrometric solution is inverted and used to locate the stars on the input frames. The position of the halos relative to the star varies across the field, but can be predicted from the star’s position within the field of view. The innermost halo (for the brightest stars, also the second halo; see Fig. 4) and a 100 pixel buffer around each ring are masked in both background subtraction and later for photometric and lensing measurements. A piece-wise linear step function model in halo-centric radius is then fit to the pixels contained within each ring, but outside the next smallest ring. This piecewise model is then subtracted from the original image, scaled to set the background to the average background level around the largest halo. The result is a flat image with the stellar core and halo rings masked out

(see the caption of Fig. 4 for details). We have verified that the inclusion of objects thus recovered does not cause any systematic shift in the weak lensing mass measurements.

### 3.1.7 Weights and masking

For each frame, we also create a weight map, following the procedure in Erben et al. (2005). The bases for the weight maps are the normalized flat-fields. Note that the star-flat correction is *not* applied to the weight maps – the weights are intended to track the relative noise across the field, which can be estimated from the variation in the original flat field.

We also use the weight maps to track bad pixels, by setting their weight to zero. We use master dark frames and flat-fields to identify hot and dead pixels, as well as image artefacts such as large dust grains. As described above, the field area outside a radius of 15 arcmin is masked due to rapidly varying PSF patterns and instability of the flat field and scattered-light correction.

In some images, the telescope autoguider blocks light from the upper  $\sim 20\%$  of the top row of chips. The exact position of this shadow moves from image to image. We automatically detect and mask this shadow by measuring the background level in the bottom  $2/3$  of the chip and comparing that to the background in the top third. We divide the upper region into subsets of  $500 \times 80$  pixels.

If the level of the background in one of these subsets is significantly below that of the lower 2/3 of the chip, that subset is masked out.

For many of the datasets, the camera was rotated by  $90^\circ$  for half of the exposures. This gives us the opportunity to recover sky area otherwise lost to saturation spikes from bright stars. The count level of saturated pixels is not constant, however. We automatically mask saturation spikes by initially identifying extended streaks of highly elevated counts in pixel columns, and then expanding these masks to include contiguous elevated regions.

We automatically mask satellite tracks by initially smoothing the image and then identifying regions on the edge of each CCD that are elevated above the background level. Satellite trails are masked when all pixels lying on a straight line connecting any two of these regions are elevated above the background as well.

Cosmic rays are detected with the standard neural network of the GaBoDS/THELI PIPELINE. Since the edges of cosmic ray hits are not always included in the mask, we expand each cosmic ray mask by one pixel in each direction.

The masking steps described above are applied to all images automatically. In the lensing band, we furthermore mask by hand the remaining artefacts pertaining to individual exposures (asteroids, off-axis reflections from bright stars, missed satellite tracks). To aid this process, we coadd the field both with median stacking and weighted mean. Comparing these images, image artefacts in individual frames become readily visible. By inverting the astrometric solution of the input frames, these artefacts can be efficiently masked on the original exposures, before the final coaddition.

Fig. 5 shows an example weight map of a coadded lensing image.

### 3.2 Final astrometry, relative photometry, resampling and coaddition

At this stage, the data reduction switches from run-specific processing to being set-specific, where *set* refers to all observations of a given (cluster) field.

We run SCAMP a second time on all images of a given cluster, for each image passing the linear solution of the first pass through SCAMP (Sect. 3.1.3) as the astrometric starting point. This time, all saturated objects are removed from the catalogs. This second pass further improves the internal astrometric solution – the positions of objects are now consistent across all frames to within a fraction of one pixel (Fig. 6). Such high astrometric precision is critical for coadding the lensing images, as well as color measurements across pixel-matched images. At the same time, SCAMP determines the relative zero-points of exposures in the same filter – this was not possible in the first pass, where saturated objects were included, and where we had not yet applied the star-flat. Note that as part of the star-flat correction, we also determine possible zero-point offsets between the CCDs (see Paper II).

The images (and weight maps) are resampled onto a common astrometric grid (i.e. common CRVAL and CDELTA WCS keywords) using SWARP (Bertin et al. 2002). The pixel scale is homogenized to 0.2 arcsec. We use the Lanczos3 kernel for resampling because of its robust signal conservation and noise properties. The flux in all images is scaled to an exposure time of 1s. From the resampled images, we create several coadded images: Firstly, for each filter, we create a median-stacked image from all available exposures (unless the seeing is worse than 1.5 arcsec, or an exposure has previously been rejected, e.g. because the sky background is as high as the saturation limit, or there are bright reflections over the entire frame). In the detection band, this will also be the detec-

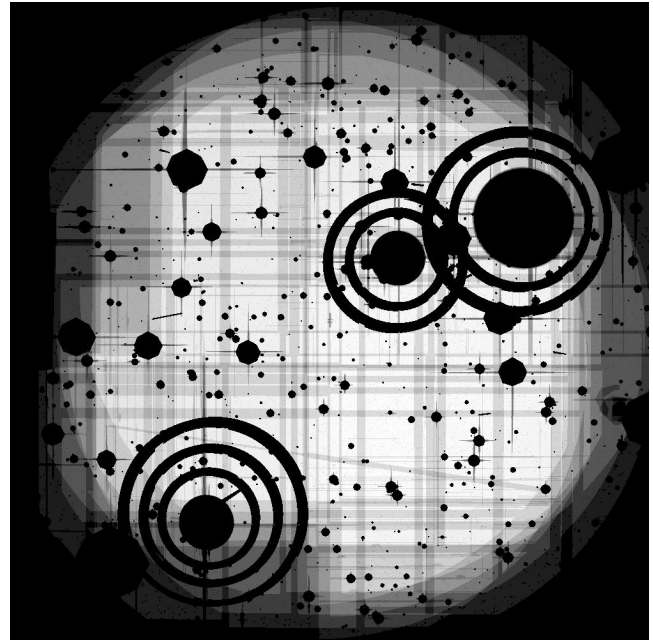


**Figure 5.** An example of a weight map for a coadded lensing image. The weight map tracks the total exposure time accumulated at each pixel (but scaled for photometric offsets). A total of eight exposures were coadded; the camera was rotated by  $90^\circ$  after the first four. The brightness scales linearly with the weight. Black areas (no weight) have been masked on the final image – these are mainly bright stars, and the rings around the brightest stars. The uneven weight across the image is readily apparent. At the field edges, this is largely because the two orientations cover different parts of the sky. For the lensing images, we reject the chip in the top left corner because of its noticeable charge transfer inefficiency – this is visible as the low weight regions at the top left and bottom left parts of the image. Also discernible as areas of lower weight are the chip gaps, saturation spikes from bright stars, and masks due to a satellite and image artefacts.

tion image (see Sect. 4.1), for the other filters, this image serves primarily visualization purposes.

Due to the heterogeneous nature of our dataset, we choose to measure object fluxes on individual exposures (see Sect. 4.2). For this purpose, we create one image for each exposure, pixel-matched to the deep median image; i.e. we resample the chips from a given exposure onto the common grid.

At this point we select the lensing band(s), where our aim is to select an image with good seeing, great depth, and uniform observing conditions. The only filters considered for this purpose are those with the highest through-puts, i.e.  $V_J$ ,  $R_C$ ,  $I_C$ ,  $i^*$ , and  $i^*$ . Exposures from SuprimeCam configurations 8, 9, and 10.3 are not considered. In many fields, the choice is clear, but in some, we select more than one lensing band. We currently make no effort to combine shape measurements from different bands. However, these cluster fields with multiple lensing bands provide an excellent opportunity for testing our methods across different observations. For some lensing bands, observations from more than one night are available. If the seeing / exposure time is markedly different, only images from the night with the best seeing / greatest depth are used. If the observations are of similar quality, we use all exposures for the lensing image, where we create one coadded image per night and per camera rotation angle, as well as a coadded image from all nights (see Sect. 5.5 for further discussion). For each lensing image, the input exposures are coadded with a weighted coaddition (according to the weight maps described in Sect. 3.1.7), which provides the opti-

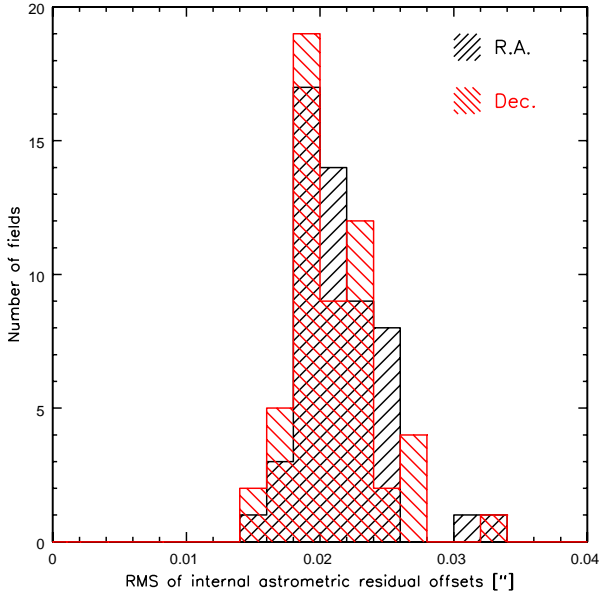


**Figure 6.** Illustration of the astrometric accuracy achieved with SCAMP. For each cluster field, SCAMP computes the RMS of all internal astrometric residuals, across all input catalogs. This figure shows the distribution of these RMS values for all our fields after the second SCAMP pass (Sect. 3.2). The RMS along the R.A./Dec. axis is shown as a black/red histogram, for objects with  $S/N > 50$ . The remaining astrometric uncertainty is only  $\sim 1/10^{\text{th}}$  of the pixel scale.

mal noise properties under homogeneous conditions. These images are used for the shape measurements (see Sect. 5).

In the coadded lensing image, we mask features that could compromise the shape measurements. Our images contain large numbers of saturated stars, for which the PSF wings are visible and need to be masked. The majority of these can be masked automatically by placing template masks according to entries in the USNO-B1 catalog (see Erben et al. 2009, for details); the rest are masked manually. Large foreground galaxies are also masked. Our images are deep, and in some of them, faint Galactic cirrus is visible. We mask the brightest knots of this nebulosity in the fields that are most affected. We track the masks in the weight image.

## 4 CATALOG CREATION AND PHOTOMETRY

### 4.1 Object detection

We detect objects in the median coadded image of the lensing band using SExtractor. Detecting on the median coadd instead of the lensing image (which is coadded with a weighted coaddition) has the advantage of avoiding residual spurious artefacts (e.g. asteroid trails, cosmic ray hits), which may have been missed at the masking stage. Also, since only the highest-quality exposures were used for the lensing image, the median image is deeper for some cluster fields, facilitating object detection. At this stage, we aim to construct a catalog that is highly complete and correctly deblends faint objects close to one another. This allows us to later test for possible biases in the shear measurements from close neighbors (see Paper III). Meeting these requirements requires fairly aggressive SExtractor settings (DETECT\_MINAREA=15, DETECT\_THRESH=0.5,

ANALYSIS\_THRESH=0.5, DEBLEND\_NTHRESH=64, DEBLEND\_MINCONT=0.00001), as also noted by other authors (e.g. Capak et al. 2007; Guo et al. 2013). This catalog provides our initial master catalog. For the following photometry measurements, we make heavy use of SExtractor’s dual-image mode to measure photometric properties of the objects in this catalog on other images (Sect. 4.2). It will also form the basis of the object catalogs for which we measure weak-lensing shape parameters (Sect. 5.2). These subsequent steps automatically reject any spurious detections, both as part of the shape measurement process, as well as with requirements on signal-to-noise and object magnitudes in at least three filters (see Paper III for more details).

### 4.2 Flux measurements

Our dataset is heterogeneous. Some cluster fields have been observed repeatedly in different seeing conditions and/or different configurations of SuprimeCam. Furthermore, most of the SuprimeCam configurations have at least two different types of CCDs in the array, leading to chip-dependent effective response curves. To properly account for these effects, we measure photometric properties from individual exposures.

Each exposure has been resampled onto an image that is pixel-matched to the detection image. For photometry, these images are convolved to a common PSF size using a Gaussian kernel (see Erben et al. 2009, for details). The final seeing is chosen to be the largest seeing encountered in any single exposure of the cluster in all filters. However, if the seeing differences are large, the Gaussian scaling of the PSF is expected to break down. We therefore adopt the strategy of the EDisCS photometry (White et al. 2005) and limit the maximum PSF size to be no more than the seeing of the detection image plus  $0.3''$ . Exposures with seeing worse than this are also included, but are not convolved.

For photometric redshifts, robust color measurements are essential. Due to possible color gradients, galaxy colors need to be measured from flux measurements of the same physical aperture on the galaxy. We measure fluxes within a fixed aperture of  $3''$ . This is the same aperture as was used in the COSMOS survey (Capak et al. 2007). The COSMOS survey forms the basis of our reference deep field for computing cluster masses. Furthermore, we used the COSMOS photometry and redshifts to extensively test the quality of our photometric redshifts, and our algorithm to incorporate individual redshift probability distributions (see Paper III).

The flux measurements for each object from the different exposures are combined according to filter, configuration, and chip type (e.g.  $R_C$ , configuration 8, SITe chip type). Individual measurements where any of the object pixels are masked are rejected. We measure the zero-point offsets between exposures with high signal-to-noise objects, and adjust the relative zero-points accordingly; note that the zero-point is no longer a single number for an exposure, but is specific to the chip type. The flux measurements for an object of the same filter, configuration and chip type are combined with an iterative clipped mean, where measurements are rejected if they are discrepant by more than  $5\sigma$  from the mean (where  $\sigma = \sqrt{\sigma_{\text{meas}}^2 + \sigma_{\text{mean}}^2}$  accounts for both the error on the measurement  $\sigma_{\text{meas}}$ , scaled for the presence of correlated noise, and the error on the mean,  $\sigma_{\text{mean}}$ ). Each galaxy may have multiple measurements in each filter corresponding to the different configurations and CCD types with which it was observed. These are treated effectively as different filters throughout the analysis (although the color terms between different chip types are small).

### 4.2.1 Photometric calibration

For most of our observations, standard star observations are not available, and even when they are, these exposures are usually too sparse to allow a robust calibration of the zero-points as a function of airmass and color terms. A large number (25/51) of our fields fall into the SDSS footprint, allowing us to calibrate the observations directly. To do so, we identify stars from the lensing image (where a clean selection of high signal-to-noise, but unsaturated, stars is essential for the PSF correction; see Sect. 5.3). For these stars, we calibrate the absolute zero-point of a single filter (typically the  $R_C$  band from the 10\_2 configuration, excluding the top left CCD, which has a different type from the other nine CCDs) against the SDSS photometry, taking into account the color terms (due to different response functions) between the SDSS filters and the filter/chip combination that we calibrate here.

For all the MACS clusters that are not in the SDSS field, we took calibration exposures to allow calibration against SDSS: we took short (3s) exposures of the cluster field, and a field within SDSS at similar airmass, back-to-back in time. We can thus calibrate the short exposure of the SDSS field, and transfer the zero-point to the cluster exposure. The deeper exposures are then calibrated with respect to the short cluster exposure.

Of the remaining 11 fields without SDSS calibration, we have MegaPrime  $r'$  imaging for six. All MegaPrime imaging is photometrically calibrated by taking short calibration exposures during photometric conditions (Magnier & Cuillandre 2004). For these fields, we can therefore use the  $r'$  band as the absolutely photometrically calibrated band.

This leaves five clusters without SDSS or MegaPrime calibration data. From the calibrated fields, we find that the extinction-corrected  $R_C$  zero-point is relatively stable, within  $\lesssim 0.1$  mag. Using data from the CFHT SkyProbe monitor<sup>1</sup>, we confirmed that the outliers in this distribution correspond to nights with noticeable extinction due to cloud cover. SkyProbe shows that the  $R_C$  band exposures of the five uncalibrated clusters were taken on photometric nights; hence we can assign the typical zero-point to these images.

Photometric redshifts are based mainly on the spectral energy distribution of object; therefore, the color calibration, i.e. the zero-point differences between bands, is more critical than the absolute photometric calibration. In the presence of a spectroscopic training set for the observed fields, several implementations of photometric redshift estimators allow one to solve for the relative zero-points of the different bands. Since we have spectroscopic redshifts only for a minority of our fields, we instead calibrate the relative zero-points by matching the colors of stars against the expected stellar color-color locus (e.g. High et al. 2009). In Paper II we describe this procedure in detail. We find that we can calibrate the relative zero-points to sufficient precision that our photometric redshifts have negligible bias.

## 5 SHEAR MEASUREMENTS

One of the key ingredients of weak-lensing measurements is robust shear estimation of faint background galaxies. We use the KSB method developed by Kaiser et al. (1995), Luppino & Kaiser (1997), and Hoekstra et al. (1998), with modifications by Erben

et al. (2001). We choose the KSB method because it has been extensively tested (Heymans et al. 2006; Massey et al. 2007) and, despite its simplicity, performs robustly on a variety of data.

### 5.1 KSB in a nutshell

Here we provide a brief summary of the KSB algorithm. For a more in-depth review, see e.g. Bartelmann & Schneider (2001).

In the KSB algorithm, the complex ellipticity  $e$  for each object is estimated from the second moments  $Q_{ij}$  of the object's light distribution  $I(\theta)$ :

$$e = e_1 + ie_2 = \frac{Q_{11} - Q_{22} + 2iQ_{12}}{Q_{11} + Q_{22}} \quad , \quad (1)$$

where

$$Q_{ij} = \int d^2\theta I(\theta) W_{r_g}(|\theta|) \theta_i \theta_j \quad , \quad (2)$$

and  $W_{r_g}$  is a Gaussian weight function of width  $r_g$  (we use the FLUX\_RADIUS measured by SExtractor for  $r_g$ ; see the discussion in Schrabback 2008). Following Erben et al. (2001), we use the same weight function to define a signal-to-noise ratio of each object:

$$S/N = \frac{\int d^2\theta I(\theta) W_{r_g}(|\theta|)}{\sigma_{\text{sky}} \sqrt{\int d^2\theta W_{r_g}^2(|\theta|)}} \quad , \quad (3)$$

which captures the uncertainty in the shape measurement. This shape-specific signal-to-noise measure is different from the flux signal-to-noise: for our data, objects with a shape  $S/N$  of  $\sim 3$  are highly significant detections with  $\text{FLUX\_ISO}/\sigma_{\text{FLUX\_ISO}} \sim 30$ .

Gravitational lensing has two effects on the observed shapes of background galaxies: the convergence  $\kappa$  scales the image of a background object isotropically, and the shear  $\gamma$  stretches it anisotropically. The combined effect is the reduced shear:

$$\mathbf{g} = \frac{\gamma}{1 - \kappa} \quad . \quad (4)$$

In the limit of small shear ( $g \ll 1$ ), and only small anisotropy of the telescope's point spread function (PSF), the (seeing-convolved) intrinsic ellipticity  $\hat{e}^0$  of an object is transformed to the observed ellipticity

$$\mathbf{e} = \hat{e}^0 + P^g \mathbf{g} + P^{\text{sm}} \mathbf{q}^* \quad ; \quad P^g = P^{\text{sh}} - P^{\text{sm}} (P^{\text{sm}})^{-1} P^{\text{sh}} \quad . \quad (5)$$

The stellar anisotropy kernel  $\mathbf{q}^*$  describes the anisotropic component of the PSF; the smear polarizability tensor  $P^{\text{sm}}$  describes the susceptibility of an object to the PSF anisotropy (and largely depends on the apparent object size); and the shear polarizability tensor  $P^{\text{sh}}$  describes the object response to the shear.  $P^{\text{sm}}$  and  $P^{\text{sh}}$  are measured from an object's third and fourth order moments. The starred quantities of these tensors are measured on stars; but note that the weight function must be adjusted to the object size (Hoekstra et al. 1998).

$\mathbf{q}^*$  is measured from stars (for which the gravitational shear  $\mathbf{g}$  and intrinsic ellipticity  $\hat{e}^0$  vanish), so that the galaxy ellipticities can be corrected for the anisotropy of the PSF. The reduced shear is then

$$\mathbf{g} = (P^g)^{-1} (\mathbf{e}^{\text{aniso}} - \mathbf{e}^0) \quad ; \quad \mathbf{e}^{\text{aniso}} = \mathbf{e} - P^{\text{sm}} \mathbf{q}^* \quad . \quad (6)$$

The source ellipticity  $\mathbf{e}^0$  is of course not known. KSB instead returns

$$\hat{\mathbf{g}} = (P^g)^{-1} \mathbf{e}^{\text{aniso}} \quad . \quad (7)$$

<sup>1</sup> <http://www.cfht.hawaii.edu/Instruments/Elixir/skyprobe/>

Because galaxies are randomly oriented (at least to the precision required for cluster weak lensing), the average ellipticity of an unlensed population of galaxies vanishes:  $\langle e^0 \rangle = 0 = \langle (P^{\text{E}})^{-1} e^0 \rangle$ . Hence, the justification for KSB is that the expectation value  $\langle \hat{g} \rangle$  is an estimate of  $g$ .

Since the trace-free part of the  $P^{\text{E}}$  tensor is much smaller than the trace, we follow Erben et al. (2001) and make the approximations

$$(P^{\text{sm}})^{-1} P^{\text{sh}} \rightarrow \frac{\text{Tr}[P^{\text{sh}}]}{\text{Tr}[P^{\text{sm}}]} =: T^* \quad ; \quad (P^{\text{E}})^{-1} \rightarrow \frac{2}{\text{Tr}[P^{\text{E}}]} \quad (8)$$

which also reduces sensitivity to noise (Heymans et al. 2006).

## 5.2 Shape measurements and star selection

For the shape measurements, we first run SExtractor in dual-image mode, with the median coadded image as the detection image, and the image coadded for lensing (coadded with a weighted average) as the second, “measurement”, image. This step mainly serves the purpose of obtaining the SExtractor FLUX\_RADIUS(=  $r_g$ ) measurement for each object on the actual lensing image, while retaining the same object selection and identification as for the photometric catalogs.

For objects with  $0.5 \leq r_g \leq 10$  we measure the ellipticities as described above with the code ANALYSELDAC (Erben et al. 2001). Larger objects are unlikely to be background galaxies; while smaller objects are predominantly spurious detections.

ANALYSELDAC also provides a more robust measure of the half-light radius,  $r_h$ . We select stars for the PSF correction in a diagram of magnitude vs.  $r_h$ , where stars with sufficient signal-to-noise, but which are not saturated, form a well-defined sequence (Fig. 7). The star selection is refined by fitting the PSF anisotropy across the field with a second-order polynomial, and rejecting  $5\sigma$  outliers (for the actual PSF correction we use a higher-order polynomial; see next section). The number of stars varies considerably in the sample, from 300 to 3000 per field. With the roughly circular field of view of radius  $\sim 15$  arcmin, this corresponds to  $0.4 - 4$  stars arcmin $^{-2}$ , with the typical number density being  $\sim 1$  star arcmin $^{-2}$ . The stars selected here also form the basis of the relative photometric calibration between bands via the stellar color-color locus (see Paper II); the color-color diagrams confirm that the stellar sample selected here is fairly clean.

## 5.3 PSF anisotropy correction

Correcting for the PSF anisotropy,  $q^* = (P^{\text{sm}})^{-1} e^*$ , is essential, as it can mimic shear. However, the PSF can only be measured at discrete locations in the image plane, namely at the positions of suitable stars. We measure  $q^*$  for the selected stars (see above), and fit a polynomial function to the spatial variation in both components (Fig. 7).

An important question here is whether the PSF is stable across chip boundaries – this is the case if the CCDs are sufficiently coplanar. If the CCDs are mounted at different heights, the focus position and hence PSF shape changes abruptly across the CCD boundary. On a single exposure, or coadded images with dither patterns of the size of the gaps between chips, this could be accounted for by fitting the PSF variation for each CCD separately. For our data, however, the dither patterns are significantly larger, and for most fields, the camera has been rotated by  $90^\circ$  between exposures. We have tested for “jumps” of the SuprimeCam PSF in images with excellent seeing and a large density of stars (see App. B1) and find that

in configurations 10\_1 and 10\_2 (used for shape measurements), the CCDs are remarkably coplanar – there are no measurable discrete PSF jumps across chip boundaries. (This is not the case in early data, another reason to disregard those data for lensing purposes.) Hence, the PSF pattern can be corrected across the full field of view, without the need to correct on a chip-by-chip basis.

The PSF of SuprimeCam (and MegaPrime) can vary considerably over the field of view, even in single exposures. We fit the entire field with a single polynomial, but find that usually a high order polynomial is required (from fourth order up to a limit of tenth order). Other authors instead divide the field into subsets and fit these with second order polynomials, but since this creates discontinuities in the PSF, we prefer the single, higher-order polynomial.

We developed a number of criteria to judge the quality of the PSF correction, and to choose the minimum polynomial order required to achieve a good fit. This process is described in App. B2.

Note that we calculate  $q^*$  using the weight function of each star (i.e.  $r_g = r_g^*$ ). As Hoekstra et al. (1998) have argued, all quantities in Eq. 5 should be measured with the same weight function as the object (galaxy) to be corrected. However, if the anisotropy of the PSF does not vary with isophote level (which is a good approximation for many ground-based instruments),  $q^*$  is independent of the width of the weight function. Measuring it with the stellar weight function automatically reduces the noise in this measurement, making the PSF measurement more robust. We find no systematic shift in shear measurements when measuring  $q^*$  with the galaxy weight function, consistent with the results of Heymans et al. (2006).

## 5.4 PSF isotropy correction

The isotropic part of the PSF (expressed as the  $P^{\text{E}}$  tensor), circularizes object shapes. If inadequately corrected, this can lead to a dilution of the shear measurement. For the calculation of  $P^{\text{E}}$ ,  $T^* = \text{Tr}[P^{\text{sh}}]/\text{Tr}[P^{\text{sm}}]$  needs to be measured from stars. This quantity is sensitive to the size of the weight function and therefore must be measured with the weight function appropriate for the object to be corrected, and within the same aperture used for the object. Furthermore,  $T^*$  can vary spatially, as the size of the PSF can vary within the field of view. In well-focused exposures, the PSF tends to be smaller at the center of the field of view than towards the edges. If this is left unaccounted for, it can lead to systematic biases in the radial shear profile, and thus the cluster mass measurement. We measure  $T^*$  at discrete values  $r_g^b$  of the weight function size over the range  $0.33 \leq r_g^b \leq 10$ , in  $0.33$  pixel increments. For each weight function scale, we fit the spatial variation of  $T^*$  with a second-order polynomial across the images, which suffices to capture the variation (Fig. 8). For each object, we then assign  $T^*$  according to the fit for  $r_g^b$  closest to the object size  $r_g$ . The trend of  $T^*$  with object size is linear for objects larger than the PSF, but shows an upturn at  $r_g \lesssim 1.5$  px (right panel of Fig. 8). Since this upturn is likely an artefact, we reject objects with  $r_g < 1.5$  px. (Note that in the lensing analysis, we apply an additional, stricter size criterion based on  $r_h$ ; see Paper III.)

## 5.5 Coaddition and PSF correction – influence on cluster mass measurements?

Apart from spatial variation, the SuprimeCam PSF is also temporally variable. Both the telescope and camera contribute to the anisotropy of the PSF; i.e. in some fields, rotating the camera by

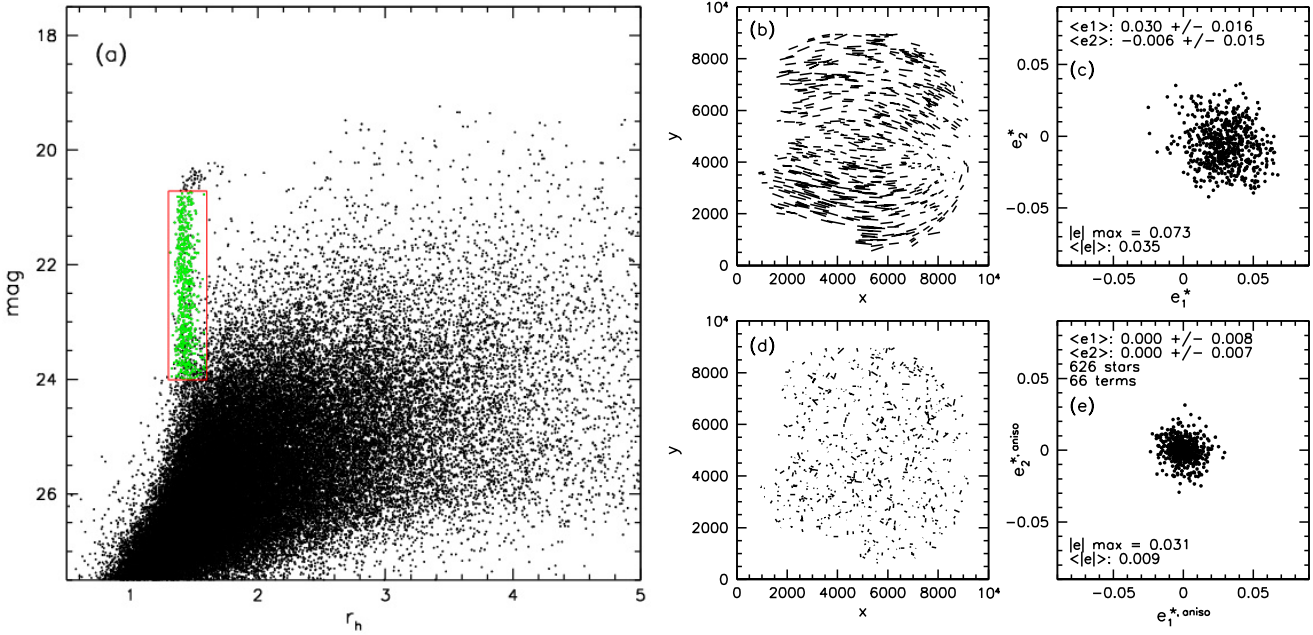


**Figure 7.** Illustration of the star selection and PSF anisotropy correction, shown for the MACSJ0025.4–1222  $V_J$  field. Panel (a) shows the magnitude - radius diagram for all objects in the catalog. The stellar sequence is clearly visible at  $r_h \sim 1.4\text{px}$ . The preselection of stars is shown as the red box. Stars that are not rejected as significant outliers in the initial second-order polynomial fit are shown in green. In the figures on the right, we illustrate the correction itself. Panel (b) shows the uncorrected stellar ellipticity pattern: at the position of each star, the measured ellipticity is indicated as a line with a length proportional to  $|e^*|$ , with orientation  $\phi = 0.5 \arctan(e_2^*/e_1^*)$ . Panel (c) shows the distribution of  $e_1^*$  vs.  $e_2^*$  values. Panel (d) shows the residual ellipticities after correcting the PSF pattern with an eighth-order polynomial (see Fig. B3); the distribution of corrected  $e_1^*$  and  $e_2^*$  values is shown in panel (e). Note that for the SuprimeCam data, the size of the coadded output image ( $33\text{arcmin} \times 33\text{arcmin}$ ) is larger than the area covered by the input frames – because we mask pixels more than  $15\text{arcmin}$  from each exposure center, the non-zero-weight part of the output image appears roughly circular. The “missing corners” visible in panels (b) and (d) are due to the top-left chip “w67c1”, which has noticeable CTI and lower QE than the other chips, and therefore is rejected.

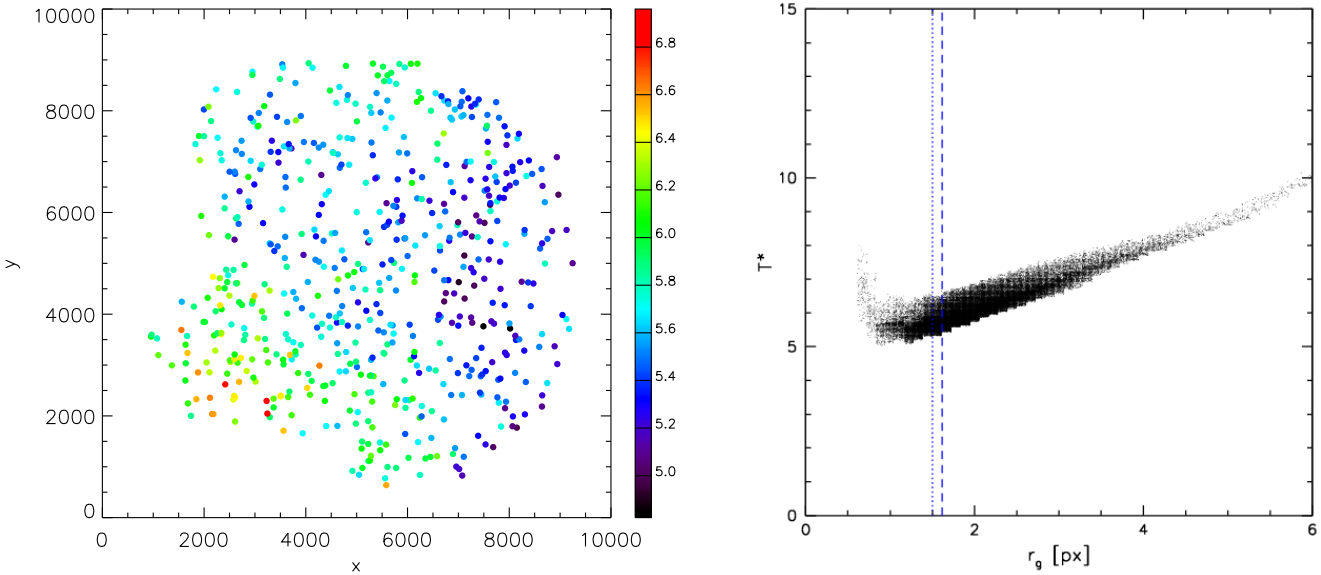


**Figure 8.** Illustration of the PSF isotropy correction as a function of position and object size, for the MACSJ0025.4–1222  $V_J$  field. The left panel shows the variation of  $T^* = \text{Tr}[P^{*\text{sh}}]/\text{Tr}[P^{*\text{sm}}]$  across the field of view. At the position of each star, we indicate  $T^*$ , measured with a weight function of width  $r_g = 0.6\text{arcsec}$ . Note the 20% variation across the image, which we fit with a second-order polynomial. The right panel shows  $T^*$  as a function of object size, evaluated at each object position with the appropriate weight function. The spread in  $T^*$  at a given  $r_g$  reflects the spatial variation shown on the left. We impose a minimum size criterion of  $r_g > 1.5\text{px}$  (illustrated by the dotted blue line), to avoid the upturn at smaller scales. For comparison, the median  $r_g$  of stars is indicated by the dashed blue line.

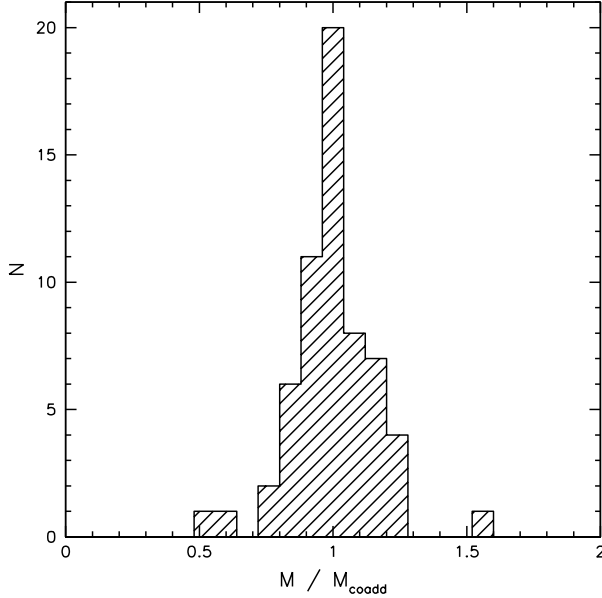


**Figure 9.** The distribution of ratios between masses measured from lensing images coadded from single nights and rotations and masses measured from the full coadded lensing image (using all available nights and rotations). The masses were measured with the “color-cut” method; see Paper III. No bias is introduced into the mass measurements by using full coadded lensing images. The scatter in mass ratios is largely due to limited number statistics in some images; e.g. the “outliers” with values of 0.5 and 1.5 were measured from less than 2000 galaxies.

90° causes stellar ellipticities to reverse sign (in sky coordinates), and sometimes the PSF pattern remains largely intact through rotation. Since for a significant fraction of our data, the camera was rotated between exposures, we must ask whether the PSF of a coadded image can still be adequately corrected. The goal of our project is to measure unbiased cluster masses, and so we evaluate this issue by testing whether masses measured from coadded images are biased. We perform this test on the “worst-case” fields, where several sets with very different PSF patterns have been coadded. These are fields with excellent (but still adequately sampled) seeing ( $\sim 0.5''$ ), with camera rotation between exposures, and with exposures often taken on more than one night (note that on all but one field, the size of the seeing disk is comparable between nights due to our lensing image selection process). Within a given field, night, and rotation, the PSF pattern is relatively stable. We therefore coadd images from these subsets (i.e. for a given subset, only exposures from the same night and with the same camera rotation angle are used), and compare masses measured on these images to the image coadded from all subsets (the mass measurement is described in Paper III).

The distribution of ratios between masses measured on subsets and on the fully coadded image is shown in Fig. 9. For most comparisons, mass measurements from different coadded images agree very well: the distribution clearly peaks at 1, with a median ratio of 0.993, indicating that using the full coadded image does not lead to biased cluster mass measurements on average.

We furthermore investigate the influence of the PSF correction on the mass measurements. For this purpose, we compare masses determined with shear measurements corrected only with a second order polynomial to those using the polynomial order determined according to the process described in App. B2 (almost all sixth,

eighth, or tenth order). The change in measured mass when the PSF is not adequately corrected is best described by an offset of  $\sim -5 \times 10^{13} M_{\odot}$ , measured at  $2.5\sigma$  significance. For clusters in the mass range of our sample, this corresponds to mass underestimates of the order of 1–10%, illustrating the requirement of an adequate PSF correction for cluster mass measurements.

To test whether the mass measurements are robust against changes in the details of how the PSF correction polynomial is determined, we also compare mass measurements if the order of the polynomial is decreased or increased by two orders. There is no significant mass shift. The PSF correction criteria developed in App. B2 therefore are sufficient for our purpose.

## 5.6 STEP calibration

A crucial element of the analysis is to calibrate the shear measurement bias inherent to KSB methods, which typically underestimate the shear (Erben et al. 2001). Any underestimate of the shear will result in a direct underestimate of the cluster mass. Fortunately, the cosmic shear community has led efforts to provide calibration datasets for shear measurement methods with the Shear TEsting Programme (STEP, Heymans et al. 2006; Massey et al. 2007). We use the simulations from the STEP 2 project (Massey et al. 2007) to calibrate the estimator  $\hat{g}$  to the true input shear  $g$  as a function of the  $S/N$  and size of each galaxy. In Paper III we describe the characterization of the full probability distribution of  $p(\hat{g}|g)$ ; here we summarize the results applicable when considering simple averaging of the shear estimators.

### 5.6.1 Shear measurement bias as a function of $S/N$

Fig. 10 shows the results for the average multiplicative shear bias, determined from the STEP data, as a function of the signal-to-noise ratio measured in the STEP images,  $(S/N)_{\text{STEP}}$ . The bias is highly dependent on  $(S/N)_{\text{STEP}}$ , in the sense that it is consistent with a constant value above  $(S/N)_{\text{STEP}} \gtrsim 7$ , and increases significantly (in magnitude) for objects with lower  $(S/N)_{\text{STEP}}$ . We find a slightly smaller correction for PSF model “C” with  $0.8''$  seeing, than for PSF “A” with  $0.6''$ , possibly because the PSF is better sampled. Of the PSF models tested in Massey et al. (2007), these are the most appropriate; since we discard the edges of the field, the highly elliptical PSF “D” and “E” are less applicable.

This behavior, with an approximately constant shear bias above a threshold signal-to-noise, and large negative bias below the threshold, is very similar to other KSB implementations (Massey et al. 2007). In particular, it is very similar to the “TS” implementation of Schrabback et al. (2007) tested in STEP-2. In Hartlap et al. (2009), those authors also show the shear bias as a function of  $S/N$ . Taking into account the re-scaling of  $S/N$  due to correlated noise (see below) and the fact that TS apply a constant shear scaling of 1.08, the results are in excellent agreement (as would be expected, as both methods are based on the same implementation of KSB+ as described in Erben et al. 2001). Using all the PSF models tested in STEP-2, these authors detect and subsequently correct for a slight  $S/N$ -dependence also for large  $S/N$  (Schrabback et al. 2010). In the two PSF models we tested, we do not find evidence for such a trend with  $S/N$ , but acknowledge that we might be lacking enough statistics to do so.

Fig. 10 illustrates strikingly the need for accurate  $S/N$  estimates for each object. By requiring  $(S/N)_{\text{STEP}} > 7$ , we can ensure that we utilize only objects in the regime where the shear measure-

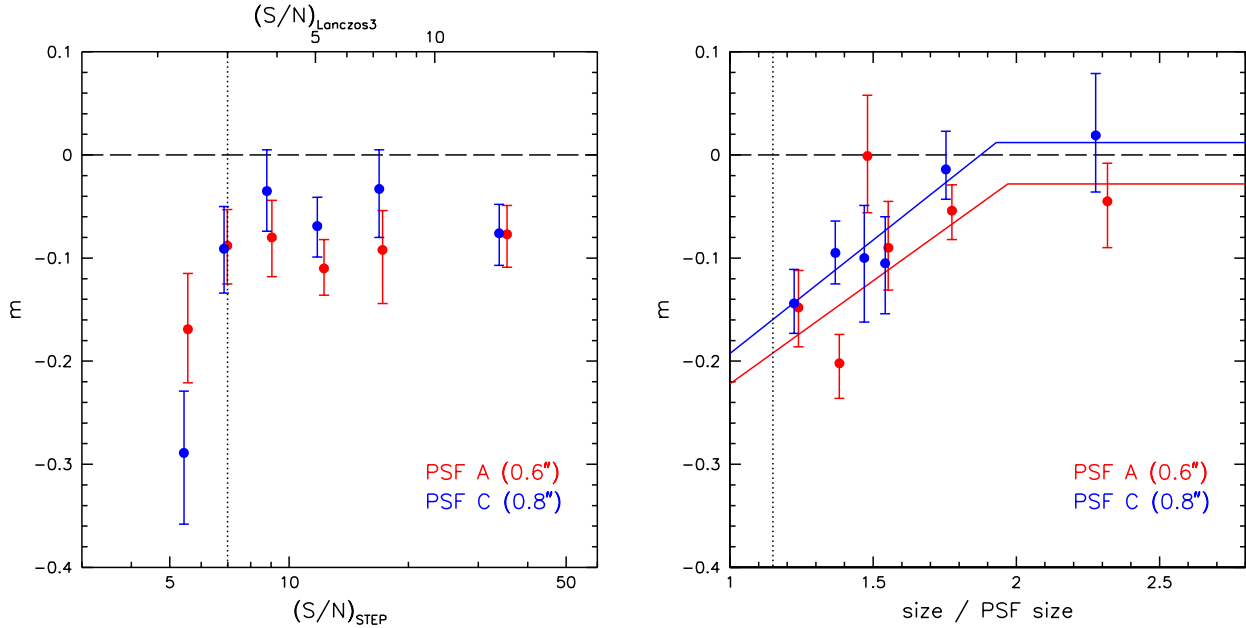


**Figure 10.** Results of our calibration of the shear measurement bias from the STEP simulations. Shown is the multiplicative shear bias  $m$  (i.e. a value of  $-0.1$  means the estimated shear is 90% of the true shear, since the additive bias is small and consistent with zero), as a function of  $S/N$  (left panel) and object size (right panel). For  $(S/N)_{STEP} \geq 7$ , the bias is approximately constant,  $m \sim -0.09$  for PSF A ( $0.6''$ ), and  $m \sim -0.06$  for PSF C ( $0.8''$ ). Below this threshold, the magnitude of the bias is significantly larger. However, because of the strong correlated noise in the STEP2 images,  $(S/N)_{STEP}$  overestimates the true signal-to-noise ratio. Our images are less susceptible to correlated noise (due to choosing the LANCZOS3 kernel for resampling; see text for details). We find that the  $(S/N)_{STEP} \geq 7$  threshold approximately corresponds to  $(S/N)_{LANCZOS3} \geq 3$  for our images, and hence impose this criterion for objects entering the shear analysis. The right panel shows the shear bias for objects with  $(S/N)_{STEP} \geq 7$  as a function of object size, in units of the PSF size (measured as the median  $r_h$  of stars selected for the PSF correction). There is a notable trend with size, in that the magnitude of the bias is larger for smaller objects. To correct for this size-dependence, we fit a piecewise linear function to the unbinned data, constrained to be a constant value for large objects. We find no statistically significant difference between corrections for the two shear components. The dotted line indicates the minimum size criterion used to reject point sources.

ment bias is robust, and does not depend sensitively on the signal-to-noise ratio.

### 5.6.2 Accounting for correlated noise

A complication with applying the STEP calibration to the actual images is that the measured noise properties (and thus  $S/N$ ) are sensitive to correlated noise. Signal-to-noise in images with correlated noise is overestimated if the estimation procedure does not explicitly account for its presence. Corrections to account for the effects of correlated noise have been made to address correlated noise in photometry measurements (Casertano et al. 2000; Masci 2009) and in shape measurements (Schrabback et al. 2007).

In the actual data, the correlated noise stems from the resampling process, but the choice of the Lanczos3 kernel minimizes the amount of correlation introduced. In the STEP2 images, correlated noise was artificially introduced by smoothing with a gaussian kernel.

The effects of correlated noise are most pronounced when only a few pixels are involved in a measurement, and is asymptotic to a constant correction at a large number of pixels. To quantify the effects of correlated noise on  $S/N$ , we created artificial images with Gaussian noise approximating the noise properties of our images, and 10000 “objects” (for simplicity, we use normal distributions of a fixed width) at equal spacing in the images. We then resampled these images using the same kernel as our actual images, as well as applying a Gaussian smoothing kernel, as was done for the STEP2 images.

By comparing the distribution of measured  $S/N$  values for the shape measurement procedure for the two resampled images, we are able to determine the scaling factor between the signal to noise measure on our images and the STEP2 images. To test for aperture size effects, we repeat this procedure for objects with FWHM of 2 pixels to 18 pixels. There is only a weak dependence of the scaling on galaxy size over the range of galaxies accepted into our analysis. We estimate the scaling of  $S/N$  between our images to the STEP images to be  $\approx 2.3$ . The threshold in shear bias that we see in the STEP images at  $(S/N)_{STEP} \sim 7$  thus corresponds to  $S/N \sim 3$  for our data. By requiring  $S/N \geq 3$ , we therefore robustly select only objects for which the average shear calibration bias is not a strong function of  $S/N$ .

The significance  $\nu$  that is used in the IMCAT implementation of KSB is larger than the  $S/N$  measure by a factor of 3.5 (Erben et al. 2001); our  $S/N$  cut therefore corresponds to  $\nu \gtrsim 11.5$ . Compared to other weak-lensing studies, this  $S/N$ -cut is relatively conservative (see e.g. Table A1 of Heymans et al. 2006). It is also worth keeping in mind that the lensing- $S/N$  is lower than the detection significance (see Sect. 5.1).

### 5.6.3 Assigning the correct $S/N$ ratio

A further practical consideration is necessary to assign the correct  $S/N$  for each object, because ANALYSELDAC assumes a constant sky noise level when calculating  $S/N$  (Eq. 3). For our images, with large dither patterns, rotation between exposures, and ample mask-

ing, this is certainly not the case, as illustrated by a typical weight map shown in Fig. 5.

We correct for this by scaling the reported  $S/N$  according to the local weight. The sky noise used to calculate  $S/N$  from Eq. 3 is the average RMS of the sky background as measured by SExtractor on the lensing image. The relative sky noise scales with exposure time as  $\sigma_{\text{sky}} \propto 1/\sqrt{t_{\text{exp}}}$  (recall that our images are normalized to a 1s exposure time). The weight map tracks the effective exposure time per pixel; therefore we can recover the actual  $S/N$  by scaling the reported value by the square root of the ratio between the average non-zero weight and the local weight. By comparing with measurements made on smaller image cut-outs with constant noise, we have verified that this recovers the true  $S/N$  to within a few percent, enough precision to identify galaxies above the threshold  $S/N$  value.

#### 5.6.4 Shear measurement bias as a function of object size

In the regime where the average shear measurement bias does not depend on  $(S/N)_{\text{STEP}}$ , we test for dependence on the size of the object (in units of PSF size, Fig. 10). We find that the shear underestimate is worst for objects just larger than the PSF, and is smallest for well-sampled objects. This is expected and consistent with other KSB implementations (Massey et al. 2007). We therefore express the correction to be applied to the shear measurement as a function of object size ( $r_h$  as returned by ANALYSELDAC, scaled by the size of the PSF, defined as the median  $r_h$  of stars selected for the PSF correction). Fig. 10 illustrates the best-fit correction; in Paper III this process is described in more detail, including how the uncertainties in the shape correction are propagated to the mass measurements.

## 6 CLUSTER IMAGES AND MAPS OF SHEAR, OPTICAL LIGHT, AND X-RAY EMISSION

High-quality lensing catalogs represent one of the main ingredients for cluster mass measurements, which are fully described in Paper III. With the lensing catalog at hand, however, the two-dimensional shear field in each cluster field can also be reconstructed to identify mass overdensities. Together with optical and X-ray images, these provide a multi-wavelength view of each cluster field. For each cluster, we present such a multi-wavelength view in a field of  $24' \times 24'$ , consisting of a three-color image, contours of the mass distribution as recovered from the shear field, the surrounding large-scale structure as traced by the light from red sequence galaxies, and the cluster X-ray emission. MACSJ1621.3+3810 is shown as an example in Fig. 11, the maps for the other clusters are presented in Appendix C.

### 6.1 Aperture mass maps and shear profiles

The lensing maps are calculated with the aperture mass statistic ( $M_{\text{ap}}$ ; Schneider 1996). The aperture mass has the advantages that it is insensitive to the mass-sheet degeneracy, which is a concern for clusters that subtend a significant part of the field of view, and that it can be calculated from shear estimates in a finite region. We use the filter and weight function advocated by Schirmer et al. (2004) and Hettterscheidt et al. (2005), which follows the expected shear profile of an NFW profile in order to maximize the signal of real halos. The scale of the filter is chosen such that the outer radial limit corresponds to 1.5 Mpc at the cluster redshift. Following Hettterscheidt et al. (2005), we fix the second free parameter of

the filter function to  $x_c = 0.15$ . For these reconstructions, bright galaxies and galaxies on the red sequence are excluded from the lensing analysis. The  $M_{\text{ap}}$  contours shown in Fig. 11 and App. C are signal-to-noise contours, defined as in Schirmer et al. (2004).

For each cluster we furthermore show the azimuthally averaged tangential and radial shear profiles.

### 6.2 Light maps

To display the distribution of cluster galaxies, and the surrounding large-scale structure, we identify the red sequence galaxies at the cluster redshift. The photometry catalog that we use in the lensing analysis has been optimized to be highly complete for faint background galaxies; however, this leads to “shredding” of bright, large galaxies due to excessive deblending. For studying the population of cluster galaxies, the requirements on the photometry catalog are different: bright galaxies must be robustly identified and measured, whereas completeness at the faintest magnitudes can be compromised. Hence, we create a second set of catalogs with different SExtractor settings tuned to the measurements of cluster members (DETECT\_MINAREA=12, DETECT\_THRESH=1.5, ANALYSIS\_THRESH=1.5, DEBLEND\_NTHRESH=64, DEBLEND\_MINCONT=0.0001, FILTER\_NAME = gauss\_1.5\_3x3.conv).

We identify the red sequence with three filters, i.e. in two color-magnitude diagrams (CMDs). Only galaxies that are on the red sequence in both CMDs are considered red sequence members (see also Paper III). Especially for clusters at higher redshifts, where the contrast of the red sequence to the back-/foreground population is low, this strategy boosts the purity of the red sequence sample.

If the Brightest Cluster Galaxy (BCG) is not on the red sequence, as is the case in several cool-core clusters (Sect. 7.2), it is added to the red sequence population. From the red sequence galaxy sample, we create luminosity-weighted maps by smoothing with a Gaussian kernel.

### 6.3 X-ray emission maps

Every cluster in our sample has been followed up with the *Chandra* X-ray observatory. The analysis of these data is described in M10 and Mantz et al., in prep. For the purpose of these maps, we adaptively smooth the processed (and if available, merged from several exposures) images. Point sources are detected as described in Ehlert et al. (2013) and masked before smoothing.

### 6.4 Correspondence between optical, X-ray, and lensing structures

All clusters are detected in the lensing maps with at least  $3\sigma$  significance with the 1.5 Mpc  $M_{\text{ap}}$  filter; the median significance is  $6\sigma$ . For clusters with low significance, the  $M_{\text{ap}}$  measurement tends to be compromised by masks of bright stars located close to the cluster center, reducing the number of available background galaxies and signal-to-noise (see also Sect. 7.1).

The correspondence between the lensing-detected peaks and the optical and X-ray detections is generally very good, as is expected for massive clusters with high-quality data. The X-ray emission clearly indicates the most massive structure in the field; in a few fields, secondary clusters at the same redshift (e.g. in the MACSJ0911.2+1746 field) or at higher redshifts (e.g. in the

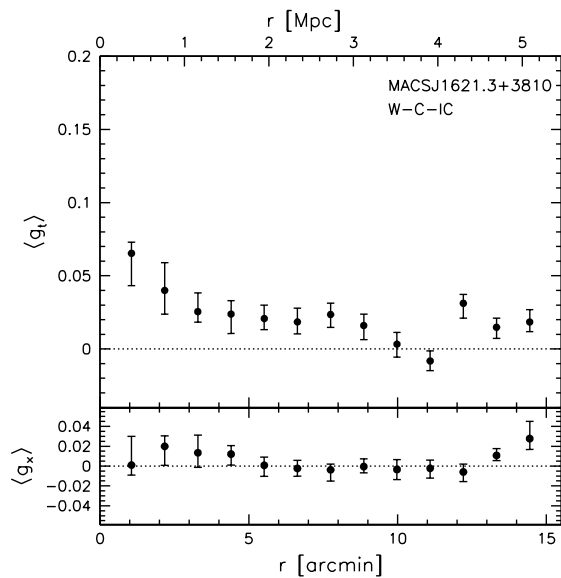
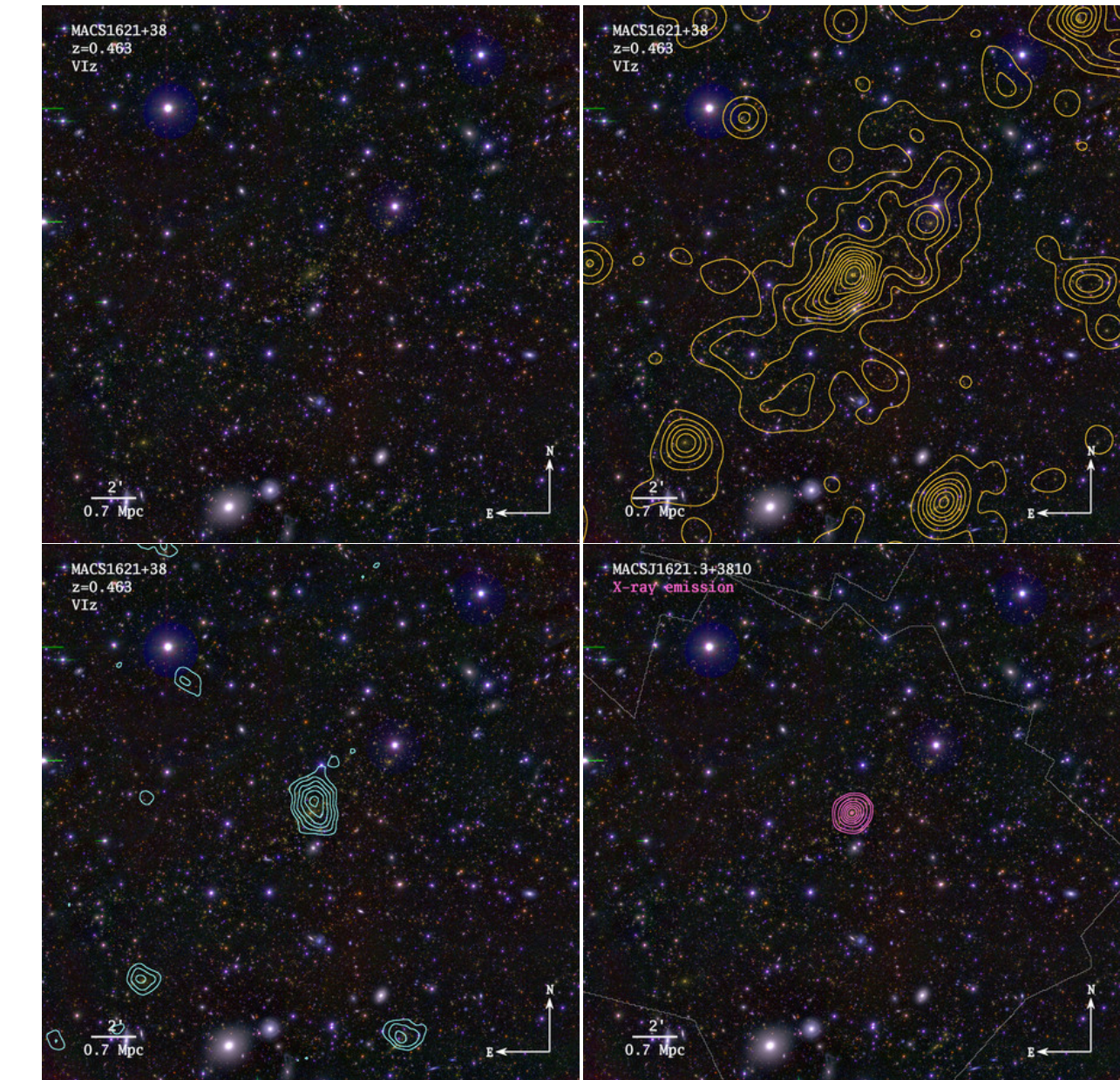


**Figure 11.** The cluster MACSJ1621.3+3810 ( $z = 0.463$ ). Each panel above shows the  $24' \times 24'$  optical image composed of the SuprimeCam  $VJICz^+$  observations. The yellow contours in the top right panel indicate the distribution of galaxies on the cluster red sequence, smoothed with a gaussian of  $3'$  width. The blue contours in the bottom left panel illustrate the aperture mass map, starting at  $2.5\sigma$  and increasing by  $0.5\sigma$  increments, reconstructed from the  $R_C$  lensing image. The outer radius of the  $M_{\text{ap}}$  filter function corresponds to 1.5 Mpc at the cluster redshift. In the bottom right panel, the pink contours indicate the X-ray emission. The white, thin contour illustrates the edge of the Chandra image (merged from four exposures); the flux contours are spaced on a square root scale. MACSJ1621.3+3810 is in the dynamically relaxed cluster sample of A08, though not in the cosmology sample of M10. Despite its relative high redshift and low X-ray flux, the multi-wavelength analysis reveals a wealth of information. The cluster is embedded in a large filament, running from southeast to northwest in the image. In an extension of the filament, (projected) 4 Mpc to the southeast of MACSJ1621.3+3810, a secondary, less massive cluster is seen in both the red sequence map and the lensing map. Another secondary cluster, possibly along a weaker filament, is located 4 Mpc to the south-southwest. (The third such cluster, in the northwest image corner, is detected in the  $I_C$  band lensing image.) The figure on the left shows the profile of the average tangential and radial shear (top and bottom panels, respectively) measured with respect to the X-ray centroid, which is at the center of the image. A coherent tangential shear signal is detected out to  $\sim 3$  Mpc.

MACSJ1115.8+0129 field) are also visible in the X-rays. These secondary clusters tend to be detected in the lensing map as well, typically as  $\sim 3 - 5\sigma$  peaks.

The optical light maps highlight the large-scale structure surrounding the target cluster. Several clusters appear to be embedded in filaments of several Mpc length (e.g. MACSJ1115.8+0129, MACSJ2228.5+2036, RX J1347-1145, MACSJ1621.3+3810). In all fields, other groups and smaller clusters at the same redshift as the main cluster are visible. A number of these are also detected in the lensing maps. Even by eye, the large scatter between optical luminosity and lensing significance (as measured by the  $M_{\text{ap}}$  statistic) is apparent, as is expected due to the measured scatter between lensing significance and cluster mass (Hamana et al. 2004), and optical richness and cluster mass (Koester et al. 2007). Note that, especially for low significance peaks, the lensing peak can be noticeably offset from the galaxy distribution (see below).

In a few fields, there are additional lensing peaks of  $3 - 4\sigma$  significance that are not clearly associated with luminous structure at the cluster redshift. Several of these correspond to clusters at higher redshift (e.g. the background clusters in the fields of MACSJ1115.8+0129, A697, Zw7215). Others do not correspond to clear galaxy overdensities (A697, MACSJ0717.5+3745) and may be caused by shape noise or low-mass projections along the line of sight. The frequency of occurrence of such alignment peaks that do not correspond to massive, virialized halos is consistent with expectations (Hamana et al. 2004; Dietrich & Hartlap 2010).

For all clusters targeted here, a coherent azimuthally averaged tangential shear signal is measured to large scales,  $3 - 5$  Mpc. The radial shear signal is consistent with zero, especially over the range over which we fit the tangential shear to determine cluster masses ( $0.75 - 3$  Mpc). Qualitatively, the inner part of the shear profile correlates somewhat with the dynamical state of the clusters: in ongoing mergers, the central shear profile is flat, or even decreases in the innermost bins. Since some of these have clearly bimodal mass distributions (e.g. A1758, MACSJ0025.4-1222) on scales of an arcminute, this is to be expected.

## 7 CLUSTER CENTERING

Robust estimates of the positions of cluster centers are essential to accurate mass measurements, as significant miscentering can lead to an underestimate of the weak-lensing mass. As long as the miscentering is not large compared to the scale of the cluster, however, the effect is expected to be small (Rozo et al. 2011). The potential bias can furthermore be mitigated if the inner cluster region is excluded from the measurement (Mandelbaum et al. 2010). The choice of cluster center is also relevant when comparing to simulations, since different halo center definitions, such as center-of-mass (e.g. Lacey & Cole 1994), most bound particle or potential minimum (e.g. Meneghetti et al. 2010; Hilbert & White 2010), or highest density peak (Tinker et al. 2008; Becker & Kravtsov 2011) approximate different observational definitions.

X-ray centroids generally provide the most robust measure of the cluster center. The X-ray flux scales with the square of the gas density, which in turn follows the overall mass distribution (unless temporarily separated as in the Bullet Cluster) – this makes the X-ray centroid a robust estimator of the cluster center. In dynamically relaxed clusters hosting a cool core, the correspondence between the bright X-ray core, the BCG, and the cluster center as

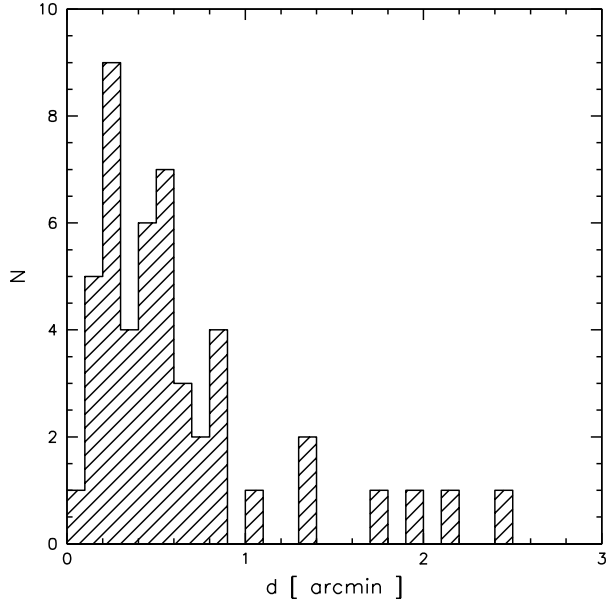


**Figure 12.** Distribution of the distance  $d$  between the X-ray centroid and the position of the peak of the weak-lensing  $M_{\text{ap}}$  map, measured in arcmin, for the 51 clusters in the sample.

indicated by strong lensing has been shown to be excellent (Allen 1998; Smith et al. 2005).

In this work, we use the X-ray centroid as the cluster center, as identified from an iterative analysis of the X-ray emission within 500 kpc, starting from the X-ray flux peak.

Here we investigate how two other possible measures of cluster centers, namely the weak-lensing peak and the position of the BCG, compare to the position of the X-ray centroid.

### 7.1 Weak-lensing peak positions

Since weak lensing is sensitive to the total cluster mass, one might be tempted to choose the peak of the weak-lensing mass map as the cluster center. However, shape noise of the background galaxies and the smoothing scale inherent to any weak-lensing mass reconstruction cause a significant dispersion of the reconstructed mass peak with respect to the true cluster center (Dietrich et al. 2012). Fig. 12 shows the measured offsets between the X-ray centroid and the peak of the  $M_{\text{ap}}$  map for our clusters. The median of the distribution is 29 arcsec, and the average is 38 arcsec. For all but seven clusters, the offset is smaller than 1 arcmin. Most of these seven clusters have large masks for bright stars close to cluster center, which affect the determination of the lensing centers. These numbers are roughly consistent with the analysis of Dietrich et al. (2012), who cite offsets between weak-lensing peaks and the cluster centers in N-body simulations. Qualitatively, this analysis suggests no significant offsets between the X-ray centroids and true cluster centers.

### 7.2 BCG positions

Cluster studies lacking X-ray data often use the position of the BCG as the cluster center. Visually, the dominant galaxy of a massive cluster can usually be unambiguously identified by its brightness, the presence of an extended stellar halo, and a flock of satellite

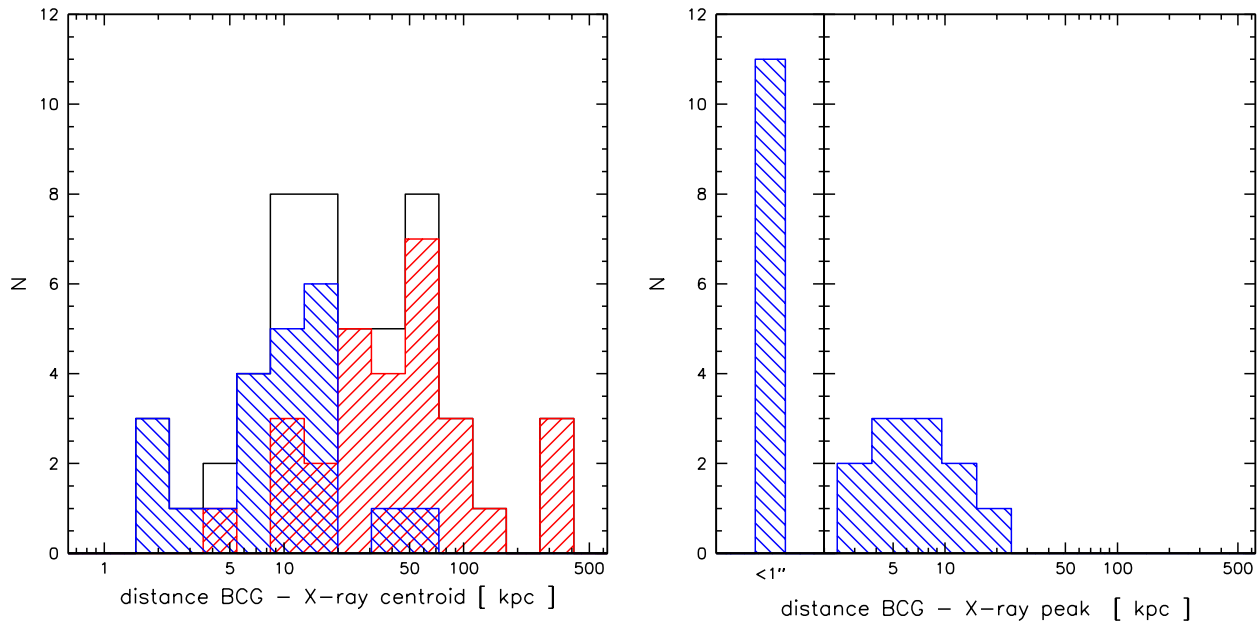


**Figure 13.** Left panel: the distribution of projected offsets between the BCG and the X-ray centroid. The black (open) histogram shows the total sample; for the blue (hatched downward) and red (hatched upward) histogram, the sample has been split into bright-core and non-bright-core clusters, respectively. There is a clear correlation between BCG – X-ray offset and dynamical state of the cluster (for which bright cores are a good proxy). Right panel: similar to the left panel, but showing the offsets between BCGs and X-ray flux peak, for bright-core clusters only. The X-ray flux peak here denotes the position of the pixel with the highest flux, after binning to 1 arcsec and accounting for X-ray point sources. For half the sample, there is no measurable offset between the positions of the BCG and X-ray peak.

galaxies. In many clusters, the BCG is indeed located near the bottom of the gravitational well of the cluster (e.g. Allen 1998; Smith et al. 2005; von der Linden et al. 2007; Best et al. 2007), but this is not always the case (Lin & Mohr 2004; Skibba et al. 2011).

For each cluster in our sample, we identify the dominant cluster galaxy in three steps: The initial BCG candidate is chosen to be the brightest galaxy on the red sequence within  $r_{500,X}$ , the radius within which the average cluster density is 500 times the critical density as determined from the X-ray data (M10). However, for cool-core clusters, the BCG may be bluer than the red sequence. As a proxy for cool-core clusters, we identify X-ray bright-core clusters by the criterion that the X-ray luminosity within  $0.05r_{500,X}$  contributes at least 17% of the total X-ray luminosity within  $r_{500,X}$  (Mantz 2009). All clusters from the A08 sample considered here are identified as bright-core clusters, as well as three additional clusters. For these clusters, if there is a brighter galaxy that is not on the red sequence, but closer to the X-ray centroid, we update the BCG choice to that galaxy. For 11 out of the 22 bright-core clusters, this is the case. Finally, we visually inspect the BCG choice, and correct it in four cases. In MACSJ1149.5+2223, the BCG appears bluer than the red sequence because of the fourth image of a strongly lensed background galaxy located close to the BCG center (Smith et al. 2009); in the other three cases, the BCG is misidentified because light from the cD halo was not correctly attributed to the BCG, but rather to superimposed objects (e.g. secondary nuclei, satellite galaxies). The blue BCGs selected for bright-core clusters all meet the visual identification criterion; i.e. they are clearly the galaxy with the largest cD envelope.

### 7.2.1 Offsets between BCGs and X-ray centroids

Fig. 13 shows the distribution of offsets between BCG position and the X-ray centroid. The offsets are small on a cluster scale: all but five are less than 100 kpc. The sample splits into two populations, one centered at  $\sim 10$  kpc, and one at  $\sim 50$  kpc. When dividing the sample into bright-core and non-bright-core clusters, it becomes apparent that the two populations correspond to these two subsamples. The cool-core dichotomy is clearly linked to the dynamical state of the cluster (e.g. Buote & Tsai 1996; Böhringer et al. 2010), and largely, the two subsamples correspond to relaxed / unrelaxed clusters. We therefore confirm previous studies that noted the correlation between BCG – X-ray offset and dynamical state of the cluster (e.g. Allen 1998; Smith et al. 2005; Bildfell et al. 2008; Sanderson et al. 2009; Hudson et al. 2010; Mann & Ebeling 2012).

There are two notable exceptions to the typically small distances between BCG and X-ray offset in bright-core clusters: in MACSJ0417.5–1154 and MACSJ0744.8+3927, the distance is of the order of 50 kpc. MACSJ0417.5–1154 is a violent merging cluster, where the X-ray emission is highly asymmetric (von der Linden et al., in prep). Although MACSJ0744.8+3927 is part of the A08 sample of relaxed clusters, it is one of the few clusters in that sample where significant substructure in the X-ray emission was noted, and excised for the hydrostatic equilibrium analysis. The offsets between the BCG and the X-ray centroid therefore predominantly reflect asymmetry of the large-scale X-ray emission.

Fig. 13 also shows the measured separations of BCGs and X-ray flux peaks, defined as the position of the pixel with the highest flux, after binning to 1 arcsec and accounting for X-ray point sources, for bright-core clusters (non-bright-core clusters by definition do not have a pronounced peak). For half the bright-core clusters, the positions are consistent to within the 1 arcsec preci-

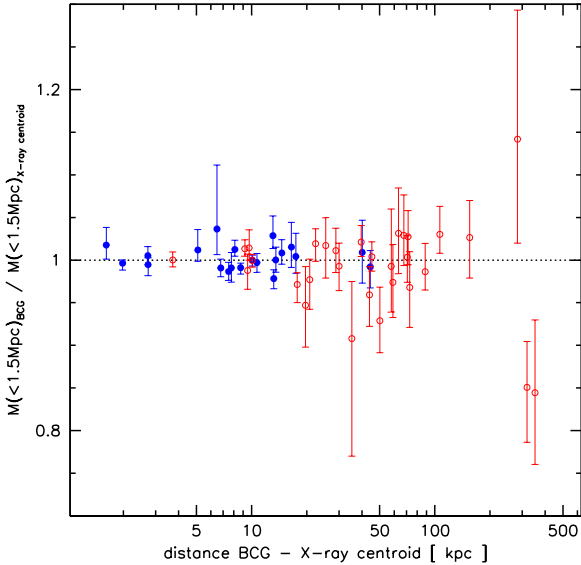


**Figure 14.** The ratios of measured masses when the BCG is chosen as cluster center to those centered the X-ray centroid (the adopted center in the subsequent analysis). Shown are the median ratios and 16<sup>th</sup> and 84<sup>th</sup> percentiles of bootstrap realizations of the source galaxy catalog. Bright-core clusters are shown in blue, solid symbols, and non-bright-core clusters as red, open symbols. The masses agree exceptionally well especially for offsets where the BCG is located within  $\leq 100$  kpc of the X-ray centroid.

sion with which we measure the X-ray flux peak. The measured offsets are generally smaller than 10 kpc. Only in clusters where the cool core is known to have substructure (MACSJ1931.8-2634; Ehlert et al. 2011), or the X-ray exposure time is short, are the offsets larger.

For non-bright-core clusters, the distribution of BCG – X-ray centroid distances extends to larger offsets (median of 49 kpc). The clusters where the offset is larger than 100 kpc have clear bimodal galaxy distributions (MACSJ0717.5+3745, A1758N, MACSJ0025.4–1222, MACSJ2243.3–0935) and/or X-ray emission with clear substructure (A370). These clusters also tend to have more than one dominant galaxy, making the choice of BCG not entirely unambiguous. Some of these are known to have complex mass distributions on scales of a few 100 kpc, associated with on-going merger activity, which clearly violate the assumption of a single, relaxed halo. However, even for these clusters, the offsets are significantly smaller than the cluster size,  $r_{500,X} \sim 1.5$ Mpc.

### 7.2.2 Implications for the lensing analysis

For our lensing analysis, we fit the tangential shear profile between 0.75 Mpc and 3 Mpc (see Paper III). The inner cluster regions, on scales larger than the observed offsets between BCGs and X-ray centroids, are thereby excluded from the measurement, and we expect any possible bias from substructure and/or miscentering to be minimal. We test this assertion explicitly by measuring cluster masses centered on the BCG, and comparing these to those measured relative to the X-ray centroid (Fig. 14). The mass measurements agree exceptionally well: the mean ratio is  $0.999 \pm 0.002$ . For our sample and methodology, miscentering therefore is not a cause of appreciable systematic uncertainty. Fig. 14 shows that for clus-

ters where the BCG is located within  $\leq 100$  kpc of the X-ray centroid, the mass measurements typically agree within 5%. For larger offsets found in bimodal clusters, where the samples of galaxies from which the lensing mass is determined become increasingly disjoint, the dispersion appears to become larger. A similar conclusion was reached by George et al. (2012), who found from stacking the weak lensing signals of X-ray identified groups in the COSMOS survey that the most massive galaxy located close to the X-ray centroid provides a good tracer of the center-of-mass within  $\sim 75$  kpc.

The typically small offsets we find between BCGs and X-ray centers should be encouraging for SZ cluster surveys, for example, which select similarly massive clusters, but where the cluster center is difficult to determine from the survey observations. When X-ray follow-up observations are not available, our results indicate that the BCG chosen from high-quality imaging observations is typically a sufficiently robust indicator for the cluster center.

For optically selected cluster samples, on the other hand, the correspondence between our results and centering strategies is less clear. The clusters in our study are not representative of the clusters found by optical surveys, which recover large samples of less massive clusters. Johnston et al. (2007) find that the probability of choosing the “wrong” BCG decreases with cluster richness, and is approximately 10% for the most massive clusters in their sample, which is in fact reminiscent of the rate of BCG identifications we manually correct (4/51). The typical offset between misidentified BCGs and the true cluster center found or expected for optical surveys (Johnston et al. 2007; Rozo et al. 2011) is on the order of 0.4 Mpc, significantly larger than even the BCG – X-ray centroid offsets we find for the most extreme bimodal clusters. However, for large-scale optical surveys it is not possible to visually vet the choice of BCG. Automated BCG identification simply based on measured brightness could fail because of noise in the measurement, lack of sensitivity to the extended, faint cD halo, over-subtraction of the sky background at cluster center, etc. Furthermore, many optical cluster finders use the red sequence to identify clusters and BCGs; however, in cool-core clusters, the BCGs are frequently bluer than the red sequence. Miscentering is expected to be a dominant observational uncertainty for optical cluster surveys (Roza et al. 2011). However, our results indicate that at least for massive clusters, this can be improved by better BCG identification – e.g. through improvements in photometric measurements, in particular better inclusion of the cD envelope, as well as allowing the possibility for BCGs to be bluer than the red sequence.

## 8 SUMMARY AND OUTLOOK

This is the first of a series of papers aimed at measuring accurate weak-lensing masses for 51 of the most X-ray-luminous galaxy clusters – the true giants in the observable Universe. The primary goal is to measure the key mass-observable scaling relations for clusters to better than 10% accuracy, a vital prerequisite for current and future cluster surveys to utilize their full statistical power. To achieve this goal, we have developed new methods and improved upon existing ones to measure accurate weak-lensing cluster masses, and have rigorously quantified the residual sources of systematic uncertainty.

The cluster sample presented here is the largest to-date for which weak-lensing masses have been measured with a homogeneous dataset and methodology. With a redshift range of  $0.15 \leq z \leq 0.7$ , and with half the clusters at  $z > 0.4$ , it extends to higher

redshifts than previous ground-based studies. However, its key distinction is the emphasis on the minimization and accurate quantification of residual systematic uncertainties, and the blind nature of the lensing mass analysis with respect to other mass proxies.

Although the intrinsic scatter of 3D weak-lensing mass measurements is large ( $\sim 30\%$ ), cluster sample sizes of  $\sim 50$  bring the statistical uncertainty on the mean cluster mass (or mean ratio of weak-lensing mass to other mass proxy) to the 5% level. Hence, systematic uncertainties should ideally be controlled to the level of a few percent in order not to limit weak-lensing mass calibration efforts. There are three main sources of systematic uncertainties for 3D mass measurements of individual clusters: the two observational challenges lie in measuring unbiased estimators of galaxy shapes, and their redshifts. The third source of systematic uncertainty lies in relating the measured shear and redshift estimates to the mass of the cluster.

In this paper, we have laid the basis for the subsequent lensing analysis, describing a robust data reduction method that aims for both excellent shape measurements and photometry measurements. We show that the shear bias of the KSB method is a strong function of signal-to-noise ratio, and a function of object size even after low signal-to-noise objects have been rejected. Assigning each object the appropriate shear calibration is critical to this work, in particular when individual photometric redshift estimates are used. We address one source of uncertainty for the relation between measured shear and cluster mass, namely the choice of cluster center. We adopt the centroid of the X-ray emission as the cluster center, and show that the location of the dominant cluster galaxy, if correctly identified, agrees well with the X-ray centroid, with a median projected offset of only 20 kpc. Only for the most extreme bimodal cluster mergers, such as MACSJ0717.5+3745 and MACSJ0025.4–1222, are the BCG and the X-ray centroid separated by  $\geq 100$  kpc. We find no systematic bias between weak-lensing mass measurements centered on the BCGs compared to those relative to the X-ray centroids. For the clusters considered here, and with our weak-lensing methodology, miscentering therefore is not a source of systematic uncertainty.

For each cluster, we show optical images and maps of the total mass distribution measured from weak lensing, cluster structure and surrounding large-scale structure as traced by red-sequence galaxies, and the extended X-ray emission. These multi-wavelength maps illustrate the large-scale structure within which each cluster is embedded, as well as possible interactions with other mass concentrations in the field and the presence of foreground and background structures.

In Paper II (Kelly et al. 2014), we detail the key methods used for accurate photometric calibration and determination of photometric redshifts. We describe how to correct position-dependent flux-zero-points from repeated observations of the same fields (and SDSS photometry, when available). We describe a number of improvements to the “stellar locus method”, allowing us to precisely calibrate the relative zero-points between filters through reference to the narrow intrinsic locus of main sequence stars in color-color space. We show that with these techniques, we recover robust photometric redshifts even in the absence of calibration data. The quality of the photometric redshifts is further illustrated with the shear-redshift scaling behind the clusters.

In Paper III (Applegate et al. 2014), we proceed to the actual mass measurements. We develop a novel Bayesian algorithm which utilizes the full photometric redshift probability distribution, and the full distribution of KSB shear estimates with respect to the true shear. We extensively test this method on the COSMOS field and

show that, in terms of the mean recovered cluster mass, the bias of our method is at most 2% over the cluster redshift range considered here. We also measure cluster masses using an improved version of the traditional “color-cut method” used in other works, which is applicable to a larger number of weak-lensing cluster datasets. We make detailed estimates of the residual systematic uncertainties of our study, arriving at a final precision of 7% on the mean cluster mass.

In subsequent papers, we will incorporate the weak-lensing mass measurements into a self-consistent cosmological framework (Mantz et al. 2010b) in order to determine improved cosmological constraints on cosmology and key astrophysical scaling relations.

Accurate and precise absolute calibration of cluster masses will be a critical requirement for future studies aimed at constraining cosmological parameters with galaxy clusters. The methodology introduced in this series of papers should be straightforwardly adaptable to other projects, utilizing optical survey data and/or targeted follow-up observations of clusters.

## ACKNOWLEDGEMENTS

We thank the anonymous referee for their careful reading of the manuscript and for comments which helped clarify the text. We especially thank them for their quick response when substituting for the original referee. We thank Peter Capak for providing updated COSMOS photometry measurements, and him and Satoshi Miyazaki for discussions about SuprimeCam data analysis. We thank Matt Becker, Andrey Kravtsov, Henk Hoekstra, Andisheh Mahdavi, and Tim Schrabback for helpful discussions on shear measurements and cluster mass estimates.

This work is supported in part by the U.S. Department of Energy under contract number DE-AC02-76SF00515. This work was also supported by the National Science Foundation under Grant No. AST-0807458. MTA and PB acknowledge the support of NSF grant PHY-0969487. The authors acknowledge support from programs HST-AR-12654.01-A, HST-GO-12009.02-A, and HST-GO-11100.02-A provided by NASA through a grant from the Space Telescope Science Institute, which is operated by the Association of Universities for Research in Astronomy, Inc., under NASA contract NAS 5-26555. This work is also supported by the National Aeronautics and Space Administration through Chandra Award Numbers TM1-12010X, GO0-11149X, GO9-0141X, and GO8-9119X issued by the Chandra X-ray Observatory Center, which is operated by the Smithsonian Astrophysical Observatory for and on behalf of the National Aeronautics Space Administration under contract NAS8-03060. DEA recognizes the support of a Hewlett Foundation Stanford Graduate Fellowship.

Based in part on data collected at Subaru Telescope (University of Tokyo) and obtained from the SMOKA, which is operated by the Astronomy Data Center, National Astronomical Observatory of Japan. Based on observations obtained with MegaPrime/MegaCam, a joint project of CFHT and CEA/DAPNIA, at the Canada-France-Hawaii Telescope (CFHT) which is operated by the National Research Council (NRC) of Canada, the Institut National des Sciences de l’Univers of the Centre National de la Recherche Scientifique of France, and the University of Hawaii. This research used the facilities of the Canadian Astronomy Data Centre operated by the National Research Council of Canada with the support of the Canadian Space Agency. This research has made use of the VizieR catalogue access tool, CDS, Strasbourg, France. Funding for SDSS-III has been provided by

the Alfred P. Sloan Foundation, the Participating Institutions, the National Science Foundation, and the U.S. Department of Energy Office of Science. The SDSS-III web site is <http://www.sdss3.org/>. This research has made use of the NASA/IPAC Extragalactic Database (NED), which is operated by the Jet Propulsion Laboratory, Caltech, under contract with NASA.

## REFERENCES

- Adelman-McCarthy, J. K., et al. 2008, *ApJS*, 175, 297
- Allen, S. W. 1998, *MNRAS*, 296, 392
- Allen, S. W., Evrard, A. E., & Mantz, A. B. 2011, *ARA&A*, 49, 409
- Allen, S. W., Rapetti, D. A., Schmidt, R. W., Ebeling, H., Morris, R. G., & Fabian, A. C. 2008, *MNRAS*, 383, 879
- Applegate, D. E., et al. 2014, *MNRAS*, 439, 48
- Baba, H., et al. 2002, Report of the National Astronomical Observatory of Japan, 6, 23
- Bacon, D. J., Massey, R. J., Refregier, A. R., & Ellis, R. S. 2003, *MNRAS*, 344, 673
- Bahcall, N. A. & Fan, X. 1998, *ApJ*, 504, 1
- Bahé, Y. M., McCarthy, I. G., & King, L. J. 2012, *MNRAS*, 421, 1073
- Bardeau, S., Soucaill, G., Kneib, J.-P., Czoske, O., Ebeling, H., Hudelot, P., Smail, I., & Smith, G. P. 2007, *A&A*, 470, 449
- Bartelmann, M. & Schneider, P. 2001, *Phys. Rep.*, 340, 291
- Becker, M. R. & Kravtsov, A. V. 2011, *ApJ*, 740, 25
- Benson, B. A., et al. 2013, *ApJ*, 763, 147
- Bertin, E. 2006, in *Astronomical Society of the Pacific Conference Series*, Vol. 351, *Astronomical Data Analysis Software and Systems XV*, ed. C. Gabriel, C. Arviset, D. Ponz, & S. Enrique, 112
- Bertin, E. & Arnouts, S. 1996, *AJ*, 117, 393
- Bertin, E., Mellier, Y., Radovich, M., Missonnier, G., Didelon, P., & Morin, B. 2002, in *Astronomical Society of the Pacific Conference Series*, Vol. 281, *Astronomical Data Analysis Software and Systems XI*, ed. D. A. Bohlender, D. Durand, & T. H. Handley, 228
- Best, P. N., von der Linden, A., Kauffmann, G., Heckman, T. M., & Kaiser, C. R. 2007, *MNRAS*, 379, 894
- Bildfell, C., Hoekstra, H., Babul, A., & Mahdavi, A. 2008, *MNRAS*, 389, 1637
- Böhringer, H., et al. 2010, *A&A*, 514, A32
- Böhringer, H., et al. 2004, *A&A*, 425, 367
- Borgani, S., et al. 2001, *ApJ*, 561, 13
- Buote, D. A. & Tsai, J. C. 1996, *ApJ*, 458, 27
- Capak, P., et al. 2007, *ApJS*, 172, 99
- Casertano, S., et al. 2000, *AJ*, 120, 2747
- Corless, V. L. & King, L. J. 2007, *MNRAS*, 380, 149
- Croft, R. A. C. & Dailey, M. 2011, *arXiv:1112.3108*
- Cypriano, E. S., Sodré, Jr., L., Kneib, J.-P., & Campusano, L. E. 2004, *ApJ*, 613, 95
- Dahle, H. 2006, *ApJ*, 653, 954
- Dahle, H., Kaiser, N., Irgens, R. J., Lilje, P. B., & Maddox, S. J. 2002, *ApJS*, 139, 313
- Dietrich, J. P., Böhnert, A., Lombardi, M., Hilbert, S., & Hartlap, J. 2012, *MNRAS*, 419, 3547
- Dietrich, J. P. & Hartlap, J. 2010, *MNRAS*, 402, 1049
- Donahue, M., Voit, G. M., Gioia, I., Lupino, G., Hughes, J. P., & Stocke, J. T. 1998, *ApJ*, 502, 550
- Donovan, D. A. K. 2007, PhD thesis, University of Hawai'i at Manoa
- Ebeling, H., Barrett, E., Donovan, D., Ma, C.-J., Edge, A. C., & van Speybroeck, L. 2007, *ApJ*, 661, L33
- Ebeling, H., Edge, A. C., Allen, S. W., Crawford, C. S., Fabian, A. C., & Huchra, J. P. 2000, *MNRAS*, 318, 333
- Ebeling, H., Edge, A. C., Bohringer, H., Allen, S. W., Crawford, C. S., Fabian, A. C., Voges, W., & Huchra, J. P. 1998, *MNRAS*, 301, 881
- Ebeling, H., Edge, A. C., & Henry, J. P. 2001, *ApJ*, 553, 668
- Ebeling, H., Edge, A. C., Mantz, A., Barrett, E., Henry, J. P., Ma, C. J., & van Speybroeck, L. 2010, *MNRAS*, 407, 83
- Ehlert, S., Allen, S. W., Brandt, W. N., Xue, Y. Q., Luo, B., von der Linden, A., Mantz, A., & Morris, R. G. 2013, *MNRAS*, 428, 3509
- Ehlert, S., et al. 2011, *MNRAS*, 411, 1641
- Erben, T., et al. 2009, *A&A*, 493, 1197
- Erben, T., et al. 2005, *Astronomische Nachrichten*, 326, 432
- Erben, T., Van Waerbeke, L., Bertin, E., Mellier, Y., & Schneider, P. 2001, *A&A*, 366, 717
- George, M. R., et al. 2012, *arXiv:1205.4262*
- Guo, Y., et al. 2013, *ApJS*, 207, 24
- Hamana, T., Takada, M., & Yoshida, N. 2004, *MNRAS*, 350, 893
- Hartlap, J., Schrabback, T., Simon, P., & Schneider, P. 2009, *A&A*, 504, 689
- Henry, J. P. & Arnaud, K. A. 1991, *ApJ*, 372, 410
- Hetterscheidt, M., Erben, T., Schneider, P., Maoli, R., van Waerbeke, L., & Mellier, Y. 2005, *A&A*, 442, 43
- Hetterscheidt, M., Simon, P., Schirmer, M., Hildebrandt, H., Schrabback, T., Erben, T., & Schneider, P. 2007, *A&A*, 468, 859
- Heymans, C., et al. 2006, *MNRAS*, 368, 1323
- High, F. W., et al. 2012, *arXiv:1205.3103*
- High, F. W., Stubbs, C. W., Rest, A., Stalder, B., & Challis, P. 2009, *AJ*, 138, 110
- Hilbert, S. & White, S. D. M. 2010, *MNRAS*, 404, 486
- Hjorth, J., Oukbir, J., & van Kampen, E. 1998, *MNRAS*, 298, L1
- Hoekstra, H. 2001, *A&A*, 370, 743
- Hoekstra, H. 2003, *MNRAS*, 339, 1155
- Hoekstra, H. 2007, *MNRAS*, 379, 317
- Hoekstra, H., Donahue, M., Conselice, C. J., McNamara, B. R., & Voit, G. M. 2011, *ApJ*, 726, 48
- Hoekstra, H., Franx, M., Kuijken, K., & Squires, G. 1998, *ApJ*, 504, 636
- Hudson, D. S., Mittal, R., Reiprich, T. H., Nulsen, P. E. J., Anderson, H., & Sarazin, C. L. 2010, *A&A*, 513, A37
- Israel, H., Erben, T., Reiprich, T. H., Vikhlinin, A., Sarazin, C. L., & Schneider, P. 2012, *A&A*, 546, A79
- Iye, M., et al. 2004, *PASJ*, 56, 381
- Jee, M. J., et al. 2011, *ApJ*, 737, 59
- Johnston, D. E., et al. 2007, *arXiv:0709.1159*
- Kaiser, N. 1984, *ApJ*, 284, L9
- Kaiser, N., Squires, G., & Broadhurst, T. 1995, *ApJ*, 449, 460
- Kelly, P. L., et al. 2014, *MNRAS*, 439, 28
- Klein, J. R. & Roodman, A. 2005, *Annual Review of Nuclear and Particle Science*, 55, 141
- Koch, A., Odenkirchen, M., Caldwell, J. A. R., & Grebel, E. K. 2003, *Astronomische Nachrichten Supplement*, 324, 95
- Koester, B. P., et al. 2007, *ApJ*, 660, 221
- Kravtsov, A. V., Vikhlinin, A., & Nagai, D. 2006, *ApJ*, 650, 128
- Lacey, C. & Cole, S. 1994, *MNRAS*, 271, 676
- Leauthaud, A., et al. 2010, *ApJ*, 709, 97
- Lin, Y.-T. & Mohr, J. J. 2004, *ApJ*, 617, 879

- Luppino, G. A. & Kaiser, N. 1997, *ApJ*, 475, 20
- Magnier, E. A. & Cuillandre, J.-C. 2004, *PASP*, 116, 449
- Mahdavi, A., Hoekstra, H., Babul, A., & Henry, J. P. 2008, *MNRAS*, 384, 1567
- Mandelbaum, R., Seljak, U., Baldauf, T., & Smith, R. E. 2010, *MNRAS*, 405, 2078
- Mann, A. W. & Ebeling, H. 2012, *MNRAS*, 420, 2120
- Mantz, A., Allen, S. W., Rapetti, D., & Ebeling, H. 2010a, *MNRAS*, 406, 1759
- Mantz, A. 2009, PhD thesis, Stanford University
- Mantz, A., Allen, S. W., Ebeling, H., Rapetti, D., & Drlica-Wagner, A. 2010b, *MNRAS*, 406, 1773
- Mantz, A., Allen, S. W., & Rapetti, D. 2010c, *MNRAS*, 406, 1805
- Marrone, D. P., et al. 2012, *ApJ*, 754, 119
- Masci, F. 2009, Aperture Photometry Uncertainties assuming Priors and Correlated Noise
- Massey, R., et al. 2007, *MNRAS*, 376, 13
- Maughan, B. J. 2007, *ApJ*, 668, 772
- Meneghetti, M., Rasia, E., Merten, J., Bellagamba, F., Ettori, S., Mazzotta, P., Dolag, K., & Marri, S. 2010, *A&A*, 514, A93
- Miyazaki, S., et al. 2002, *PASJ*, 54, 833
- Nagai, D., Vikhlinin, A., & Kravtsov, A. V. 2007, *ApJ*, 655, 98
- Navarro, J. F., Frenk, C. S., & White, S. D. M. 1997, *ApJ*, 490, 493
- Oguri, M. & Hamana, T. 2011, *MNRAS*, 414, 1851
- Okabe, N., Takada, M., Umetsu, K., Futamase, T., & Smith, G. P. 2010a, *PASJ*, 62, 811
- Okabe, N., Zhang, Y.-Y., Finoguenov, A., Takada, M., Smith, G. P., Umetsu, K., & Futamase, T. 2010b, *ApJ*, 721, 875
- Pedersen, K. & Dahle, H. 2007, *ApJ*, 667, 26
- Perlmutter, S., et al. 1999, *ApJ*, 517, 565
- Planck Collaboration, et al. 2011, *A&A*, 536, A8
- Postman, M., et al. 2012, *ApJS*, 199, 25
- Predehl, P., et al. 2010, in Society of Photo-Optical Instrumentation Engineers (SPIE) Conference Series, Vol. 7732, Society of Photo-Optical Instrumentation Engineers (SPIE) Conference Series
- Rapetti, D., Allen, S. W., Mantz, A., & Ebeling, H. 2010, *MNRAS*, 406, 1796
- Rapetti, D., Blake, C., Allen, S. W., Mantz, A., Parkinson, D., & Beutler, F. 2013, *MNRAS*, 432, 973
- Rasia, E., et al. 2012, *New Journal of Physics*, 14, 055018
- Refregier, A. 2003, *MNRAS*, 338, 35
- Regnault, N., et al. 2009, *A&A*, 506, 999
- Reid, B. A., Verde, L., Jimenez, R., & Mena, O. 2010, *JCAP*, 1, 3
- Riess, A. G., et al. 1998, *AJ*, 116, 1009
- Rozo, E., Rykoff, E., Koester, B., Nord, B., Wu, H.-Y., Evrard, A., & Wechsler, R. 2011, *ApJ*, 740, 53
- Rozo, E., et al. 2010, *ApJ*, 708, 645
- Sanderson, A. J. R., Edge, A. C., & Smith, G. P. 2009, *MNRAS*, 398, 1698
- Schirmer, M. 2013, *ApJS*, 209, 21
- Schirmer, M., Erben, T., Schneider, P., Wolf, C., & Meisenheimer, K. 2004, *A&A*, 420, 75
- Schmidt, F., Vikhlinin, A., & Hu, W. 2009, *Phys. Rev. D*, 80, 083505
- Schneider, P. 1996, *MNRAS*, 283, 837
- Schrabback, T. 2008, PhD thesis, <http://hss.ulb.uni-bonn.de/2008/1336/1336.htm>
- Schrabback, T., et al. 2007, *A&A*, 468, 823
- Schrabback, T., et al. 2010, *A&A*, 516, A63+
- Schuecker, P., Böhringer, H., Collins, C. A., & Guzzo, L. 2003, *A&A*, 398, 867
- Sehgal, N., et al. 2011, *ApJ*, 732, 44
- Skibba, R. A., van den Bosch, F. C., Yang, X., More, S., Mo, H., & Fontanot, F. 2011, *MNRAS*, 410, 417
- Skrutskie, M. F., et al. 2006, *AJ*, 131, 1163
- Slater, C. T., Harding, P., & Mihos, J. C. 2009, *PASP*, 121, 1267
- Smith, G. P., et al. 2009, *ApJ*, 707, L163
- Smith, G. P., Kneib, J.-P., Smail, I., Mazzotta, P., Ebeling, H., & Czoske, O. 2005, *MNRAS*, 359, 417
- The Dark Energy Survey Collaboration. 2005, [arXiv:astro-ph/0510346](https://arxiv.org/abs/astro-ph/0510346)
- Tinker, J., Kravtsov, A. V., Klypin, A., Abazajian, K., Warren, M., Yepes, G., Gottlöber, S., & Holz, D. E. 2008, *ApJ*, 688, 709
- Truemper, J. 1993, *Science*, 260, 1769
- Umetsu, K., et al. 2012, *ApJ*, 755, 56
- Vanderlinde, K., et al. 2010, *ApJ*, 722, 1180
- Vikhlinin, A., et al. 2009a, *ApJ*, 692, 1033
- Vikhlinin, A., et al. 2009b, *ApJ*, 692, 1060
- von der Linden, A., Best, P. N., Kauffmann, G., & White, S. D. M. 2007, *MNRAS*, 379, 867
- White, S. D. M., et al. 2005, *A&A*, 444, 365
- Wu, H.-Y., Rozo, E., & Wechsler, R. H. 2010, *ApJ*, 713, 1207
- Zhang, Y.-Y., et al. 2010, *ApJ*, 711, 1033

## APPENDIX A: EARLY CONFIGURATION PROCESSING

While most of the data included in this analysis are from configurations 10.1 and 10.2, we also use data from the earlier configurations 8 and 9. There are a number of problems associated with the early data including several cosmetic effects. The largest problem, however, is the nonlinear response of the CCDs. Since for a significant fraction of the clusters,  $R_C$  and  $I_C$  images (which are essential for galaxy color information) were taken in the early configurations, we made an effort to salvage these data.

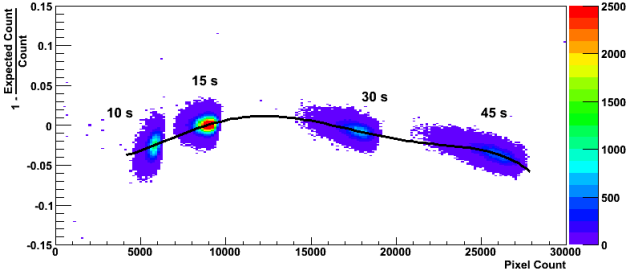
### A1 Non-linear response

Figure A1 shows the detector response to 10, 15, 30 and 45 second domeflats, normalized to the expected response from 15 second exposures. The gain varies by several percent, with a maximum gain around 10000 pixel counts above the bias level. To correct for the non-linear response, we fit a polynomial to the data shown and apply it to the observed pixel counts of science and flat fields, after overscan and bias subtraction.

We find significant evidence of variable light intensity in the corners of the focal plane for the series of domeflats used for this study. As a result, we cannot derive a correction for the corner CCDs, and we do not use those chips in the early configurations (for configuration 8, the two left-most chips; for configuration 9, the chip on the left, and the two right-most chips).

### A2 Chip defects

The chips in the early data have a considerable number of dead pixels, hot pixels, and dirt on the CCDs. Most of these can be automatically flagged in dark frames and flat-fields, and we mask the rest by hand. The two chips in the second column from the left in the array (“w9c2” and “w6c1”) have a ~10% brickwall pattern, even in the  $R_C$  and  $I_C$  bands, but this is entirely removed by flat-fielding.



**Figure A1.** The pixel response for an early data MIT/LL chip, normalized to the 15-second response, as a function of the pixel count for 10, 15, 30, and 45 second dome flats.

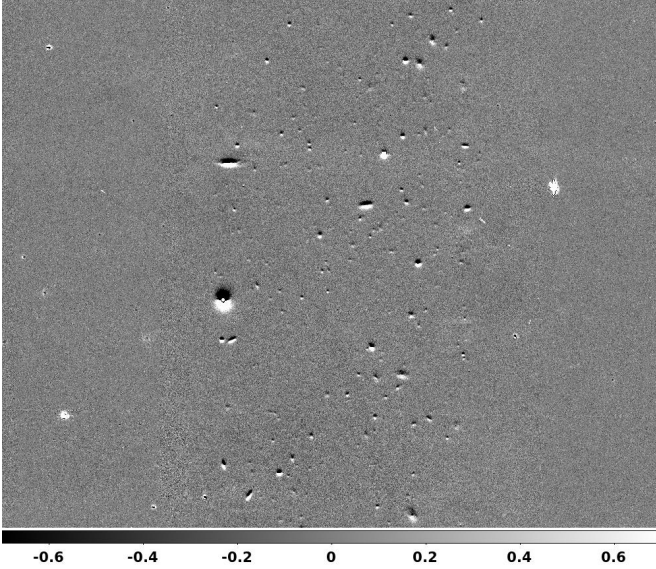


**Figure A2.** Illustration of the pixel indexing error in chip “w9c2” (DET-ID=7) of the early configurations. Shown is part of a difference image between a single exposure with this chip and the median-coadded image of the field. The area shown is  $1000 \times 800$  pixels, i.e. roughly half the chip-width. On the left and the right side of the area shown, the difference image is very smooth (apart from saturated stars), indicating good astrometric agreement. In the central  $\sim 400$  pixels, however, the objects on this chip are systematically shifted downwards by  $\sim 0.5''$ . This area runs about  $3/4^{\text{th}}$  of the length of the chip, starting from the top. The bottom end is marked by a row of hot pixels. To the sides it is flanked by  $\sim 50$ -pixel wide areas of highly correlated noise. The width of this whole area appears somewhat variable between exposures. In the process of our data reduction, we mask out the entire affected area.

The oddest defect occurs in chip “w9c2” (bottom row, second chip from the left). For  $\sim 25\%$  of the chip area, the  $y$ -coordinates of the pixels are 2-3 pixels too low, a defect that must take place during read-out. We found this from inconsistencies in the astrometric solution between this chip and other imaging of the same fields. Matching the astrometry to the remaining chip area, the objects in this strip are displaced by  $\sim 0.5''$  (Fig. A2). We mask this area.

## APPENDIX B: VERIFYING THE PSF CORRECTION

To determine the PSF anisotropy as a function of position in the image, we fit a two-dimensional polynomial to the observed ellipticity components of stars (Sect. 5.3). Fitting over the entire image (i.e.,

across chip boundaries) is warranted only if the PSF is continuous across chip boundaries. We describe how we explicitly test for PSF discontinuity in Sect. B1. In Sect. B2 we describe our criteria to choose the order of the polynomials and validate the resulting PSF correction.

### B1 Planarity of SuprimeCam

To test for discontinuities in the PSF across chip gaps, we analyze the observed shapes of stars using a shapelet decomposition (Refregier 2003). We extract “postage stamp” cutouts of regions containing a star in a given exposure, normalize each object to the same total flux, and decompose the flux distribution in terms of the (Cartesian) shapelet coefficients,

$$\phi_{n_1 n_2} = \int d\mathbf{x} I(\mathbf{x}) \Phi_{n_1 n_2}(\mathbf{x}; \beta), \quad (\text{B1})$$

where

$$\Phi_{n_1 n_2}(\mathbf{x}; \beta) = \frac{H_{n_1}(x/\beta) H_{n_2}(y/\beta)}{(2^{n_1+n_2} \pi n_1! n_2! \beta^2)^{-1/2}} \exp\left(-\frac{x^2 + y^2}{2\beta^2}\right) \quad (\text{B2})$$

and  $I(\mathbf{x})$  is the flux at  $\mathbf{x}$ , and  $H_n$  are  $n$ th Hermite polynomials. We find that maximum values of  $n_1, n_2 = 5$  (25 coefficients in total) provide an accurate measure of the object’s shape without overfitting.

The data used for this analysis are the  $R_C$ -band images of MACSJ1931.8–2634. The galactic coordinates of MACSJ1931.8–2634 are  $(l, b) = (12.5669^\circ, -20.09^\circ)$ ; i.e., it is viewed through the bulge of the Milky Way. Hence the field has a very large number of stars, and most of these stars are faint enough that they are not saturated in our exposures - this makes the field an excellent test case. We randomly separate the  $\sim 4200$  stars into equal sized training and testing samples. We then decompose the training set, and for each shapelet component fit a separate third order polynomial across the field. This produces a model of the PSF at every position in the focal plane. Figure B1 shows the results of a comparison of the PSF model and the shapes of the stars in the testing set. We divide the focal plane into several regions, and in each region we define

$$\langle \chi_v^2 \rangle = \frac{1}{N_{\text{obj}}} \sum_{i=1}^{N_{\text{obj}}} \frac{1}{N_{\text{pix}}} \sum_{j=1}^{N_{\text{pix}}} \left( \frac{\sum_{n_1, n_2} \phi_{n_1, n_2}^i \Phi_{n_1, n_2}^{i, j}(\mathbf{x}; \beta) - I(\mathbf{x})}{\sigma^{i, j}} \right)^2, \quad (\text{B3})$$

where  $N_{\text{obj}}$  is the number of stars in a bin,  $N_{\text{pix}}$  is the number of pixels in a postage stamp,  $\phi_{n_1, n_2}^i$  is the  $n_1, n_2$  shapelet coefficient of the interpolated PSF at the position of the  $i$ th star,  $\Phi_{n_1, n_2}^{i, j}$  is the integral of the shapelet function over pixel  $j$  and  $\sigma^{i, j}$  is the estimated error on the flux in that pixel. Overlaid is a map of the location of the CCD boundaries. Any PSF discontinuities would be visible as jumps or ridges in  $\chi^2$  at the chips boundaries. We observe no such jumps, and thus no evidence of PSF discontinuities across CCD gaps. Figure B2 shows  $\chi_v^2$  as a function of the distance from the center of each object to the closest CCD edge. Again, we observe no evidence of PSF discontinuities across CCD boundaries.

### B2 Quality criteria for PSF fits

For each ellipticity component, we fit a two-dimensional polynomial to the observed ellipticities of stars:  $e_i(x, y) = \sum_{j=0}^n \sum_{k=0}^j a_{i, j, k} x^k y^{j-k}$ , where  $n$  is the highest order polynomial used in the fit.

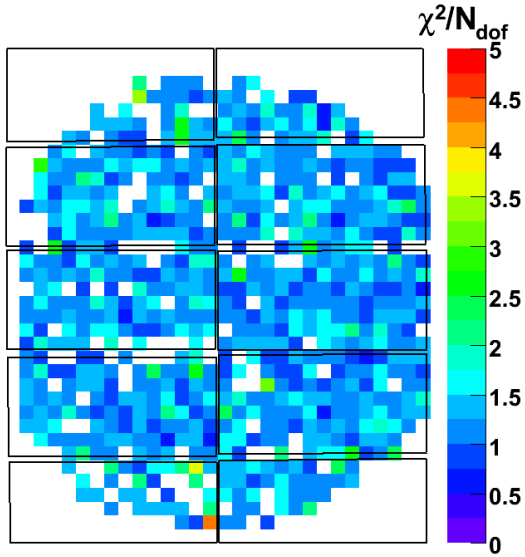


**Figure B1.** A comparison of the shapelet PSF model to the test sample of stars across the focal plane. The color scale shows the value of  $\langle \chi^2/N_{\text{dof}} \rangle$  in each bin. We observe no evidence of PSF discontinuities across chip gaps.

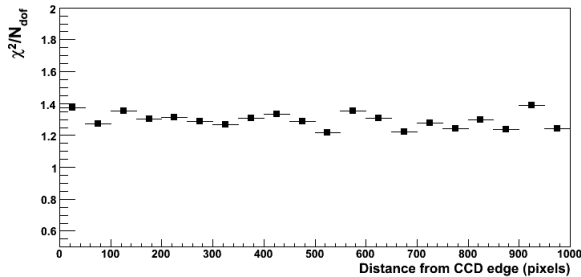


**Figure B2.** A comparison of the shapelet PSF model to the test sample of stars as a function of the distance between an object and to the nearest chip boundary. There is no evidence of the model being a worse description of the PSF near the CCD edges.

We test the goodness-of-fit in several ways. First, we verify our PSF interpolation by using a 10-fold cross validation. We randomly divide the sample of stars used for the PSF correction into ten groups. For each group, we perform a polynomial fit to the stars in the other 9 groups, and calculate the ellipticity residuals for the stars in the sample that was not used in the fit. At the end of this process, we have an estimate of the PSF ellipticity for each star without using that star in the fit. We then calculate the standard deviation of the two ellipticity component residuals,  $\sigma_{\Delta e_1}$  and  $\sigma_{\Delta e_2}$ . This technique gives an estimate of the typical difference between the estimated PSF ellipticity and the true PSF ellipticity. Typical values for  $\sigma_{\Delta e_1}$  and  $\sigma_{\Delta e_2}$  are 0.004–0.006 for SuprimeCam images and 0.003–0.004 for MegaPrime images. Images where either component is larger than 0.007 are excluded from the lensing analysis.

For cosmic shear studies, other authors have used the uncorrected stellar ellipticity - galaxy shear correlation as a probe of unmodelled PSF ellipticity (e.g. Bacon et al. 2003; Hettterscheidt et al. 2007). However, while cosmic shear fields are ideally random pointings, targeted cluster observations place the cluster center at

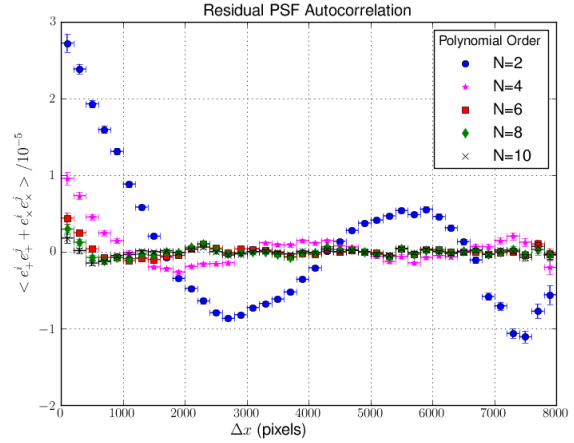


**Figure B3.** The autocorrelation of corrected stellar ellipticities after fitting the PSF in the MACSJ0025.4–1222V<sub>J</sub> field with a second, fourth, sixth, eighth, and tenth order polynomial. Note the large residual (anti-)correlation present after the second order fit. Higher order fits suppress this; in this case the eighth order polynomial meets all our criteria.

the center of the field. Since many PSF patterns, including those of SuprimeCam, display symmetry around the field center, the cluster shear and stellar ellipticity are usually correlated. This is clearly visible in the example PSF pattern shown in Fig. 7, where the measured ellipticities of the stars are tangential to the field center, much like the expected cluster shear signal.

As another test of the PSF model, we calculate the residual ellipticity autocorrelation  $\langle e_+^1 e_+^2 + e_-^1 e_-^2 \rangle$ , and require it to be either statistically consistent with zero, or less than  $10^{-5}$  over the range  $r_{ac} = (5r_{im}^2/N_{stars})^{1/2}$  and half the size of the image. Features smaller than that scale are too undersampled to be measured. A sample residual autocorrelation of stellar ellipticities is shown in Fig. B3.

To determine the appropriate maximum polynomial order ( $N$ ) to use, we repeat the analysis at every even order from  $N = 2$  to  $N = 10$ . (Most of the power comes from the even orders; the correction is very similar between a given even order and the next odd order.) The cross-validation technique provides a natural choice because  $\sigma_{\Delta e_{1,2}}$  are large when the model underfits the data (features exist in the data that are not included in the model), and when the order is too large and we overfit (including features in the model that are really statistical fluctuations). We use the fit that provides the smallest  $\sigma_{\Delta e_1} + \sigma_{\Delta e_2}$ , provided that order polynomial passes the autocorrelation requirements. We prefer cross-validation to the  $F$ -test or the likelihood-ratio test because it does not require a per-star ellipticity statistical uncertainty, which in this case can be difficult to calculate, and it provides an explicit estimate of the interpolation error ( $\sigma_{\Delta e_{1,2}}$ ). For about half the fields, we choose an eighth-order polynomial; the remainder are predominantly sixth- and tenth-order, with a few fourth-order fits.

## APPENDIX C: CLUSTER MASS, LIGHT, AND GAS MAPS

Available in electronic form at <http://mnras.oxfordjournals.org/lookup/suppl/doi:10.1093/mnras/stt1945/-/DC1>